BRAIN-INSPIRED L_p-CONVOLUTION BENEFITS LARGE KERNELS AND ALIGNS BETTER WITH VISUAL CORTEX

Anonymous authors
Paper under double-blind review

ABSTRACT

Convolutional Neural Networks (CNNs) have profoundly influenced the field of computer vision, drawing significant inspiration from the visual processing mechanisms inherent in the brain. Despite sharing fundamental structural and representational similarities with the biological visual system, differences in local connectivity patterns within CNNs open up an interesting area to explore. In this work, we explore whether integrating biologically observed receptive fields (RFs) can enhance model performance and foster alignment with brain representations. We introduce a novel methodology, termed L_p-convolution, which employs the multivariate p-generalized normal distribution as an adaptable L_p-masks, to reconcile disparities between artificial and biological RFs. L_p-masks finds the optimal RFs through task-dependent adaptation of conformation such as distortion, scale, and rotation. This allows L_p-convolution to excel in tasks that require flexible RF shapes, including not only square-shaped regular RFs but also horizontal and vertical ones. Furthermore, we demonstrate that L_p-convolution with biological RFs significantly enhances the performance of large kernel CNNs possibly by introducing structured sparsity inspired by p-generalized normal distribution in convolution. Lastly, we present that neural representations of CNNs align more closely with the visual cortex when L_p-convolution is close to biological RFs. This research shines a light on the potential of brain-inspired models that merge insights from neuroscience and machine learning, with the hope of bridging the gap between artificial and biological visual systems.

1 INTRODUCTION

Convolutional neural networks (CNNs) were initially inspired by the early discoveries from the brain's visual system, particularly the groundbreaking work of Hubel and Wiesel on receptive fields (RFs) in the primary visual cortex (V1) (Hubel & Wiesel, 1962; 1965). This laid the foundation for the Neocognitron, a precursor to CNNs, which focused on the idea of local connections (Fukushima, 1980). Building upon the backpropagation (Werbos, 1974; Rumelhart et al., 1986), and the concept of weight sharing, LeCun and his colleagues applied it to CNNs, leading to the development of the first practical CNN, known as LeNet (LeCun et al., 1989). Fueled by advancements in backpropagation, large datasets, and GPU training, the landmark success of AlexNet in 2012, which significantly outperformed existing models in the ImageNet challenge, marked a turning point for CNNs (Krizhevsky et al., 2012).

In recent times, CNNs have become a prominent model for understanding biological visual processing due to both structural and representational similarity between them (Lindsay, 2021). The CNN's architecture closely mirrors the visual system: 1) RGB channels emulate retinal computations, 2) stacked layers correspond to various visual areas (such as V1, V2, V4, IT), 3) deeper layers excel at detecting complex features, and 4) local receptive fields. In terms of representational similarity, Khaligh-Razavi & Kriegeskorte (2014) demonstrated that among 37 different computational models, CNN trained with supervision exhibited the best performance and alignment with the brain. Recently, CNNs like VGG and ResNet have become instrumental models for visual processing models in neuroscience, owing to their strong representational alignment with the brain (Khaligh-Razavi & Kriegeskorte, 2014; Simonyan & Zisserman, 2014; Shi et al., 2019; He et al., 2016; Bakhtiari et al., 2021).

While CNNs employed the concept of local connectivity inspired by the brain, they are not exact replicas. This is attributed to the contrast between the dense, uniformly connected local RFs in CNNs and the varied and sparsely connected patterns in biological neurons. This disparity poses an intriguing question that could mutually captivate both neuroscience and machine learning communities: **Would integrating biologically observed receptive fields into an artificial model result in enhanced performance and closer alignment with brain representations?**

In this paper, we introduce L_p-convolution, a novel approach that leverages the multivariate p-generalized normal distribution (MPND) to address the disparities between biological and artificial RFs (Fig. 1). Through channel-wise trainable L_p-masks in convolutional layers (Fig. 2), we explore their conformational adaptability (Fig. 3 and 4), resulting in enhanced performance in large kernel CNNs and improved alignment with biological representations (Fig. 5 and Table 1).

Overall, our contributions are:

- Introduction of MPND to model the disparity between biological and artificial RFs.
- Proposal and implementation of L_p-convolution leveraging adaptable L_p-masks.
- Demonstration of task-dependent conformational adaptability of L_p-masks with Sudoku challenge.
- Significant performance gains in large kernel CNNs in vision classification tasks.
- Improved alignment of neural representations with brain-inspired L_p-convolution.

Code, datasets, and pre-trained models are available at `https://anonymous.4open.science/r/lpconv-E39D`.

2 Bridging biological and artificial receptive fields

The distinct characteristics of dense, uniform local RFs in CNNs, as opposed to the sparse, morphologically structured connectivity patterns in biological neurons, pose a challenge for directly comparing their local RFs. To address this, we analyzed the functional connectivity patterns of both biological and artificial systems, by introducing the MPND (Goodman & Kotz, 1973). MPND is the key of our paper to bridge the conformational difference between biological and artificial RFs. While the concept of the receptive field generally encompasses sensory-level inputs and adjacent layers, in this paper, we specifically refer to **RF as the local connectivity patterns** between neurons in adjacent layers.

Multivariate p-generalized normal distribution Let s represent the d-dimensional random vectors indicating specific points within RF. s_0 is the receptive center with d-dimensional vector of fixed constants. The relative offset is given by $\Delta\mathbf{s} = \mathbf{s} - s_0$. Introducing MPND, we define the RF using as probability density function (PDF) of $\mathbf{s}$ as following:

$$\beta \exp\left(-\|\mathbf{C}\Delta\mathbf{s}\|_p^p\right), \tag{1}$$

where $\mathbf{C}$ is $d \times d$ covariance matrix, $\|\cdot\|_p^p$ denotes the L_p-norm raised to the p-th power, β is normalization factor[1], and $p \geq 1$. In Figure 1e, we show some examples of MPNDs with varying values of p and $\mathbf{C}$.

Constructing biological and artificial RFs from the functional synapses To compare the biological and artificial RFs, we first prepared the 2D offsets of functional synapses relative to the post-synaptic units in both systems: mouse V1 L2/3 and AlexNet Conv1 (Fig. 1a-d; See details in Appendix A.1 and A.2). To match the scale difference between the two systems, we standardized the relative offsets with zero mean and unit variance. For the artificial system, we prepared 4 different cases, using both ImageNet-1k pre-trained and randomly-initialized AlexNet[2] with inputs of noises or images (See inputs and corresponding RFs in Appendix A.4). We constructed 2D probability mass functions (PMFs) from the collected offsets, which we call biological or artificial RFs.

[1] $\beta = \left[(2\Gamma(1 + p^{-1}))^d \cdot \det(\mathbf{C})\right]^{-1}$ where Γ is gamma function, and $\det(\cdot)$ denotes the determinant.

[2] For clarity, we refer to *trained* as pre-trained models and to *untrained* as randomly-initialized models.

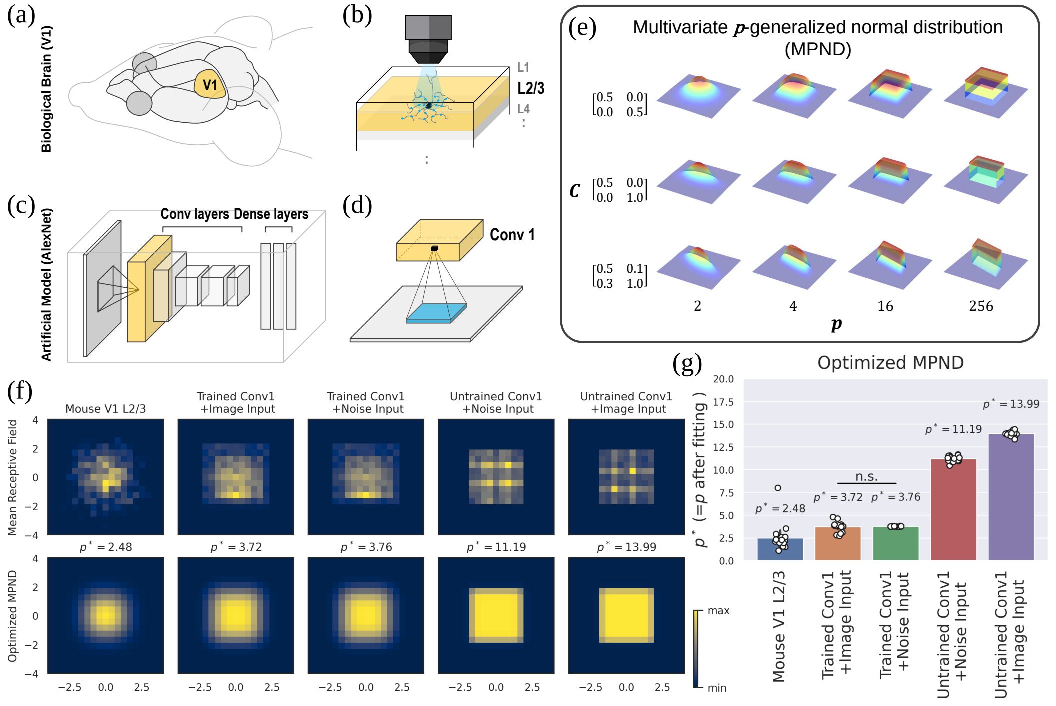

Figure 1: **Local receptive fields from biological and artificial systems can be mathematically reconciled by introducing multivariate p-generalized normal distribution** (a-b) Graphical illustration of receptive fields in V1 of mouse brain (a) at layer 2/3 (b). (c-d) Graphical illustration of receptive fields in AlexNet (c) at Conv1 layer (d). (e) Shapes of MPND with varying parameters of $\mathbf{C}$ and p. (f) Top, visualization of mean receptive fields of functional synapses in mouse V1 layer 2/3 (column 1) and AlexNet Conv1 with varying conditions (columns 2-5). Bottom, optimized MPND over receptive fields shown in the first row. (g) p after MPND optimization; Using Welch's t-test with Holm-Bonferroni's multiple comparisons correction, all possible combinations between groups were statistically significant (p-value$<$0.05) except for 'n.s.' (non-significant) denoted in the figure; n=17 for all conditions. We optimized MPND parameters of p and σ, where $\mathbf{C} = \begin{bmatrix} 1/\sigma & 0 \\ 0 & 1/\sigma \end{bmatrix}$, $\sigma_{\text{init}} = 0.5$, and $p_{\text{init}} = 2$

MPND effectively models both biological and artificial RFs For the comparison of biological and artificial RFs, we optimized parameters of p and σ in MPND (Fig. 1e, Eq. 1) over PMFs of biological or artificial RFs (Fig. 1f and g). We show that optimized p^* of functional synaptic input patterns of biological neurons were optimized at near 2 (Gaussian-distributed; See details in Appendix A.3). In contrast, the local RF pattern of pre-trained AlexNet's Conv1 was optimized at the range of $3.7 \sim 3.8$, and the untrained one was optimized at the range of $11 \sim 14$ (where input types were less effective). An intriguing observation is the decrease in the value of p for the pre-trained AlexNet's Conv1, bringing it closer to the biological RF. Based on these findings, we propose that both biological and artificial RFs can be effectively modeled with MPND, particularly within the range of $p = [2, 16]$. Given these findings, we propose to consider that the value of p close to 2 is indicative of biological RF, while a higher p represents RFs to be more artificial.

3 L_p-CONVOLUTION: INTRODUCING MPND IN THE CONVOLUTION

Based on our observation in Figure 1 artificial RFs become closer to biological RFs with training (decrease in p of MPND by ImageNet-1k training in AlexNet Conv1), we asked two intriguing questions: 1) Is it possible to improve the performance of CNNs by implementing biologically-inspired RFs on artificial models? 2) Can CNNs with RFs close to biological ones align better

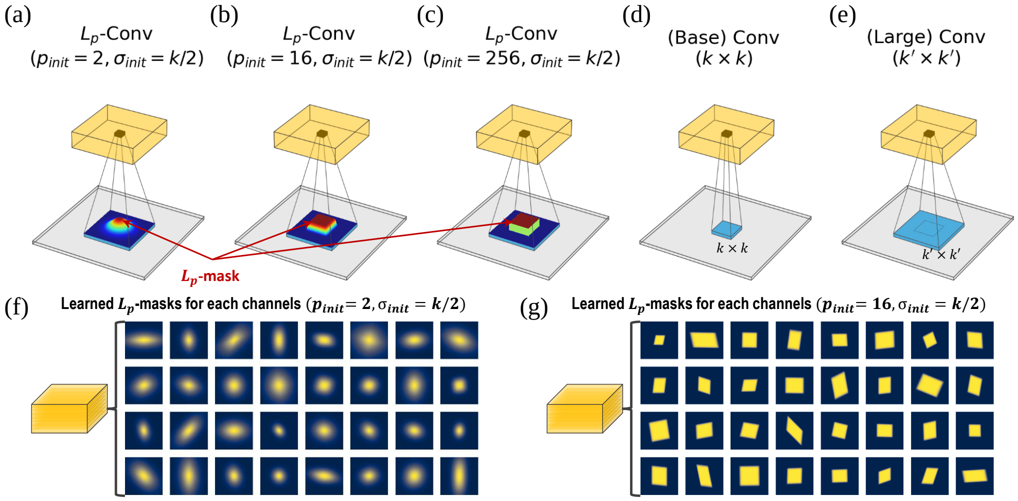
(a)
L_p-Conv
($p_{init} = 2, \sigma_{init} = k/2$)
(b)
L_p-Conv
($p_{init} = 16, \sigma_{init} = k/2$)
(c)
L_p-Conv
($p_{init} = 256, \sigma_{init} = k/2$)
(d)
(Base) Conv
($k \times k$)
(e)
(Large) Conv
($k' \times k'$)
$k \times k$
$k' \times k'$
L_p-mask
(f)
Learned L_p-masks for each channels ($p_{init} = 2, \sigma_{init} = k/2$)
(g)
Learned L_p-masks for each channels ($p_{init} = 16, \sigma_{init} = k/2$)

Figure 2: **Graphical illustration of L_p-Conv layers and visualization of learned L_p-masks after traning** (a-c) L_p-Conv layers with $\sigma_{\text{init}} = k/2$ and varying $p_{\text{init}} = \{2, 16, 256\}$; L_p-masks overlaid on kernels (red arrows). (d-e) Conventional Conv layers with the kernel size of $k \times k$ (Base) or $k' \times k'$ (Large). (f-g) Visualized 32 example learned L_p-masks from L_p-converted AlexNet Conv1 after training with Tiny Imagenet dataset

with the representation of the brain? To answer these questions, we introduce L_p**-convolution**: overlaying channel-wise trainable L_p-masks onto the kernels of CNNs.

L_p**-convolution** Here, we propose the L_p-convolution, which is compatible with various convolutions. We formulate the L_p-convolution based on the MPND in the convolutional layer by employing channel-wise L_p-masks, which are overlaid on convolutional filters (Fig. 2a-c).

First, we define the relative height and width offsets, $\Delta\mathcal{S} \in \mathbb{R}^{2\times K_h \times K_w}$ from the kernel center, $(K_h/2, K_w/2)$, as follows

$$\Delta\mathcal{S}_{\cdot,h,w} = (\Delta h, \Delta w)^T = (h - \frac{K_h}{2}, w - \frac{K_w}{2})^T \text{ for } h \in [0, K_h - 1], w \in [0, K_w - 1], \tag{2}$$

where K_h and K_w denote the kernel height and kernel width, respectively. Empirically, we utilize the normalized value between 0 and 1. It is noted that $\mathcal{S}_{\cdot,h,w} \in \mathbb{R}^2$ denotes all values corresponding to h-th height and w-th width.

Second, we propose the L_p-mask, structured mask matrix, derived from the offset and MPND. Our L_p-mask, $\mathcal{M} \in [0,1]^{C_o \times K_h \times K_w}$ for all output channel C_o, is a soft mask that is proportional to Eq. 1 without a normalization factor β as following

$$\mathcal{M}_{o,h,w} = \exp\left(-\|\mathcal{C}_{o,\cdot,\cdot}\Delta\mathcal{S}_{\cdot,h,w}\|_p^p\right), \tag{3}$$

where $\mathcal{C} \in \mathbb{R}^{C_o \times 2 \times 2}$ is the set of 2×2 covariance matrix for each output channel. In other words, L_p-mask calculates the soft mask $\mathcal{M}_{o,\cdot,\cdot}$for each o-th output channel independently, and each soft mask handles the positional correlation, height and width position, from the offset, $\Delta\mathcal{S}$. Our L_p-mask in Eq. 3 corresponds to RF in Eq. 1, when $K_h = K_W = C_o = 1$.

Third, we propose the L_p-convolution by applying L_p-mask into the convolutional weights $\mathcal{W} \in R^{C_i \times C_o \times K_h \times K_w}$, where C_i is the number of input channel. For each i-th input channel input $\mathcal{X}_i$ and convolutional filter weights $\mathcal{W}_i$, we formulate the corresponding convolution output $\mathcal{Y}_i$ as

$$\mathcal{Y}_i = \phi(\mathcal{X}_i * (\mathcal{W}_i \odot \mathcal{M})), \tag{4}$$

where ϕ is non-linear function and $*$ is the convolution operation.

We note that $\mathcal{C}$ and p are trainable parameters[3]. To ensure the positive definite property of $\mathcal{C}_o$ and satisfy the L_p-norm property with $p \geq 1$, we can employ Cholesky decomposition for $\mathcal{C}$ and value clipping for p.

As shown in Equation 4, our L_p-convolution is a generalized version of the traditional convolution. In our settings, it is noted that L_p mask converges to a binary mask as p approaches infinity. Empirically, L_p mask becomes a binary mask for sufficiently large p, as shown in Fig. 1. If all elements of L_p mask equal one, then L_p-convolution degrades to the traditional convolution. In this situation, both traditional convolution and our L_p convolution have square-shaped RFs for each layer. In other words, our L_p-convolution takes task or data-dependent RFs with varying $\mathcal{M}$ by optimizing the $\mathcal{C}$ and p as shown in Figure 2. Therefore, L_p-convolution has task-specific RFs with varying distortion, scale, and rotation levels.

In practical terms, we replaced all existing Conv2d layers in the baseline CNN model with L_p-Conv layers by applying a function called **LpConvert** to the baseline CNN model (See pseudo-code in Appendix A.13). To provide further insight into the conformational changes of L_p-masks during model training, we present examples of 32 random L_p-masks from Conv1 of an AlexNet model trained with TinyImageNet (f and g in Fig. 2).

4 Conformational adaptability of L_p-masks in Sudoku challenge

To assess the adaptability and effectiveness of evolving RFs in L_p-convolution, we conducted well-established 9×9 Sudoku-solving task (Park, 2018; Oinar, 2021; Amos & Kolter, 2017; Palm et al., 2018; Wang et al., 2019) (See experimental details in Appendix A.5). We selected the Sudoku task for its challenging nature, as it necessitates simultaneously achieving three objectives—ensuring every row, column, and box contains all numbers from 1 to 9—(Fig. 3a).

L_p-convolution in Sudoku solving: balancing square and row-column imbalances As shown in Figure 3b, the (3×3) Base model, or (7×7) $L_p^{\dagger}(p_{\text{init}} = 256)$ model exhibited a significant imbalance in Square-to-Row/Column accuracy and showed signs of overfitting after approximately 15 epochs. The (7×7) Large model demonstrated improvement in the balance of Square-to-Row/Column accuracy and overall Sudoku accuracy, possibly due to the enlarged RFs. Along with these control experiments, we tested two trainable L_p-masks with $p_{\text{init}} = 2, 16$, each of them closely resembles a biological RF ($p = 2$) and an artificial RF in ($p = 16$), respectively. In (7×7) $L_p(p_{\text{init}} = 2)$ model, we observed highly balanced Square-to-Row/Column accuracy, resulting in remarkable improvement in overall Sudoku accuracy compared to (7×7) $L_p(p_{\text{init}} = 16)$ or (7×7) Large model (red and green in Fig. 3b). We speculated that this alleviation of Square-to-Row/Column accuracy imbalance in (7×7) $L_p(p_{\text{init}} = 2)$ could be attributed to the task-dependent L_p-masks' conformational adaptability. To test this possibility, we have designed ablation experiments on (7×7) $L_p(p_{\text{init}} = 2)$ model.

Ablation of orientation selective masks reveals L_p-masks' conformational adaptability Contrary to a previous large-kernel model that introduces unstructured sparsity directly into filters (Liu et al., 2023), L_p-convolution with $p = 2$ introduces structured sparsity based on a Gaussian distribution. This approach facilitates covariance analysis of the Gaussian distribution, thereby enhancing interpretability. Using Singular Value Decomposition (SVD) on $\mathcal{C}$, we extracted three interpretable properties of scale (α), rotation (θ), and distortion (γ) (See conformational analysis in Appendix A.5). Figure 4a shows conformations of L_p-masks inverse calculated from α, θ, and γ.

Quantitative analysis of (7×7) $L_p(p_{\text{init}} = 2)$ model revealed an increase in scales when layer deepened (Fig. 4b, see visualization in Appendix A.7), with orientations of horizontal (0,180°) and vertical (90°) directions. This indicates the task-dependent adaptation of L_p-masks, which provide flexible and structured RFs in visual processing. To confirm these orientation-selective masks contribute to the balanced Sudoku-solving task, we conducted an ablation test. We classified masks with highly distorted ($\gamma > 3$) as orientation-selective masks. Among these, we selectively ablated near 90° by gradually increasing the range (close in shape with red dashed box in Fig. 4a) while

[3] C and p are updated with the standard backpropagation process. L_p-mask, $\mathcal{M}$, is dynamically generated during forward process using C and p.

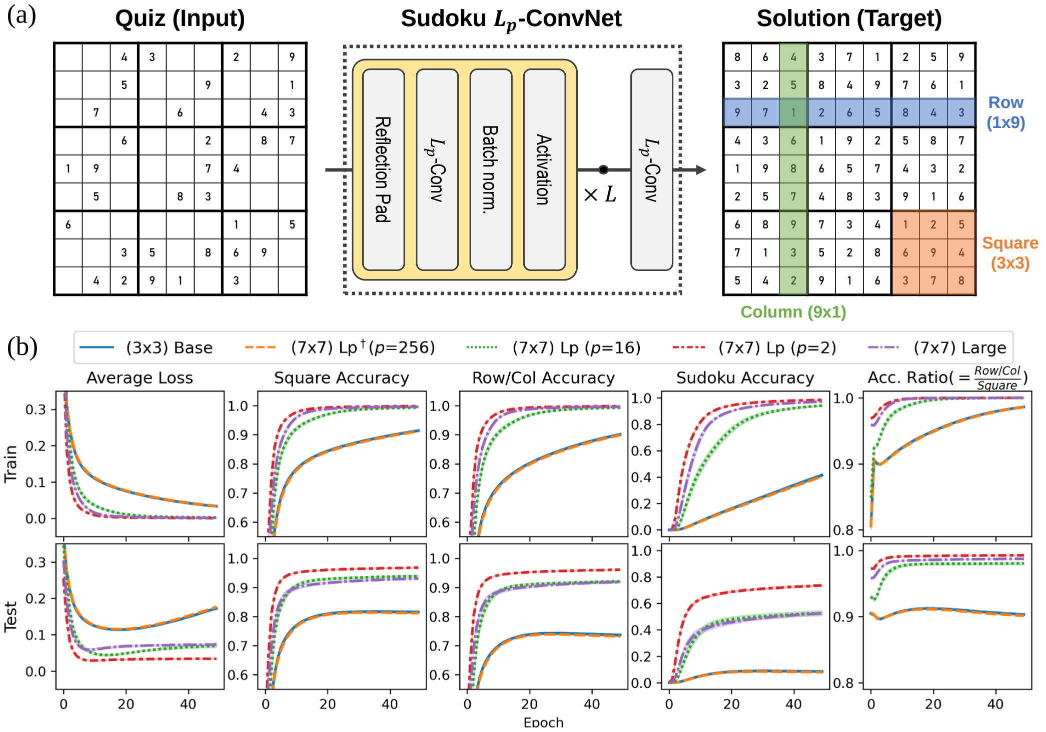

		4	3			2		9
		5			9			1
	7			6			4	3
		6			2		8	7
1	9				7	4		
	5			8	3			
6						1		5
		3	5		8	6	9	
	4	2	9	1		3		

8	6	4	3	7	1	2	5	9
3	2	5	8	4	9	7	6	1
9	7	1	2	6	5	8	4	3
4	3	6	1	9	2	5	8	7
1	9	8	6	5	7	4	3	2
2	5	7	4	8	3	9	1	6
6	8	9	7	3	4	1	2	5
7	1	3	5	2	8	6	9	4
5	4	2	9	1	6	3	7	8

Figure 3: **L_p-convolution enhances Sudoku solving efficiency by effectively balancing accuracy between square and row-column puzzles** (a) Graphical illustration of Sudoku quiz and Sudoku L_p-ConvNet; (left), example Sudoku quiz as an input; (middle), basic block repeated L times ($L =$ 10, yellow) contains sequential layers of 1) reflection padding, 2) L_p-Conv, 3) batch normalization, and 4) activation layers; (right), the example Sudoku solution as a target. In Sudoku, a 9×9 square must be filled in with numbers from 1-9 with no repeated numbers in 9x1 rows (blue), 1x9 columns (green), or 3x3 squares (orange). (b) Loss and accuracy curves during training and test sessions. '(3×3)' or '(7×7)' denotes the size kernel. '$L_p^\dagger$' denotes parameters of L_p-mask is frozen. 'Large' denotes a simple enlargement of the kernel, without a mask.

tracking changes in column and row accuracies. While row and box accuracy exhibited a consistent decrease, column accuracy sharply decreased as the θ range increased (Fig. 4c and Appendix A.8), with this trend was notable in the later layers. Together, these results indicate that the conformational adaptability of L_p-masks enables balanced learning in the Sudoku-solving task, thereby contributing to overall performance enhancement.

5 L_p-Convolution benefits large kernel CNNs in vision classification task

Next, we asked whether our designed L_p-convolution would be beneficial for enhancing the performance of historically successful CNNs. To test this, we conducted vision classification tasks (See detailed experimental settings in Appendix A.9) using the CIFAR-100 and TinyImageNet datasets on models of AlexNet, VGG-16, ResNet-18, ResNet-34, and the ConvNext-tiny (Liu et al., 2022) (Table 1). When simply increasing the kernel size, we observed a significant decrease in performance for all models except ResNet. This is consistent with a previous report of a decrease in vision classification performance with larger kernels (Peng et al., 2017).

As depicted in Table 1, when parameters are frozen with a notably large p ($p = 256$ and $\sigma = \frac{k}{2}$), L_p-Conv exhibits performance comparable to the baseline model (refer to subfigures c and d in Fig. 2 for graphical illustration). This suggests that initializing the parameters of L_p-Conv with a similar experimental configuration can contribute to the stable learning of L_p-masks, avoiding significant

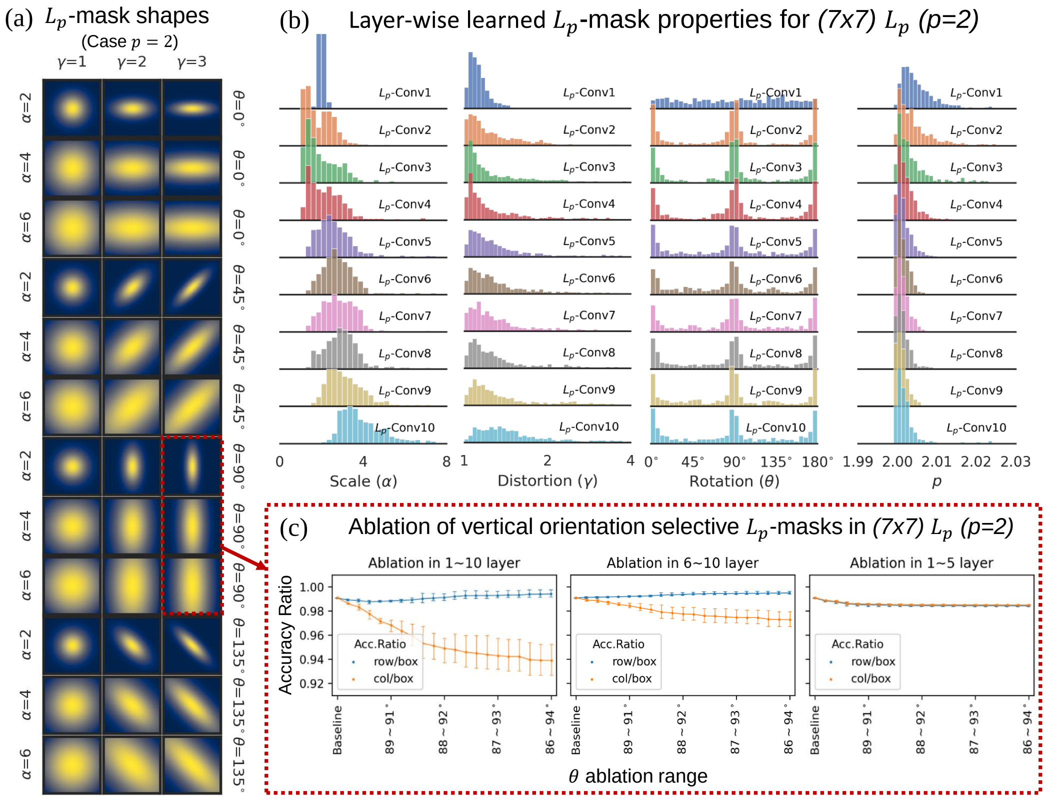

Figure 4: **Task-dependent conformational adaptation of L_p-masks** (a) The shapes of L_p-masks when $p = 2$ and varying properties of scale (α), distortion (γ), and rotation (θ), which are derived from the singular value decomposition of $\mathcal{C}$; Red box indicates column selective L_p-masks which are ablation targets in (c). (b) Layer-wise distribution of learned L_p-mask properties. (c) Selectively ablation of L_p-masks near 90° by gradually increasing the ablation; Ablation in all 10 L_p-conv layers (left), first 5 layers (middle), and last 5 layers (right) respectively.

performance degradation compared to the baseline model. Notably, in contrast to the large kernel models, all instances of L_p-Conv, regardless of the value of p_{init}, exhibit stable performance gains, as indicated in Table 1. Intriguingly, the condition $p_{\text{init}} = 2$ (which is close to biological RFs) recorded the highest performances, ranking first in seven out of ten cases and second in two. This observation suggests that employing L_p-convolution to increase the kernel size can enhance the performance of historically successful CNN models as well as the recent models, particularly when $p_{\text{init}} = 2$, which aligns closely with biologically observed RFs. This underscores the potential benefits for CNNs from incorporating brain-inspired structured sparsity and flexible RF adaptability.

6 Representational similarity analysis between L_p-CNNs and visual cortex

Figure 5a illustrates our approach to assessing the alignment of representations between biological and artificial systems. We utilized the standardized dataset from Allen Brain Observatory (de Vries et al., 2020), which uses 118 images of Natural Scenes and corresponding neural activities recorded from the mouse visual cortex (VC). Our method builds upon established Representational Similarity Analysis (RSA) techniques (Khaligh-Razavi & Kriegeskorte, 2014; Nguyen et al., 2020; Mehrer et al., 2020; Devereux et al., 2013; Diedrichsen & Kriegeskorte, 2017), to compare the representations of CNNs (Bakhtiari et al., 2021; Shi et al., 2019) (See details in Appendix A.11).

Table 1: Top-1 performance on the CIFAR-100 and TinyImageNet datasets in CNNs are reported with 5 trials (mean±std). The symbol † indicates that both $\mathcal{C}$ and p are frozen parameters during training. $k' = 2 \times \lceil \frac{k}{2} \rceil + k$. For all L_p-Conv layers, $\mathcal{C}$ was initialized with $1/\sigma_{\text{init}}$ of diagonals and 0 of off-diagonals, where $\sigma_{\text{init}} = k/2$. Statistical comparison results using Welch's t-test with the base model are marked as follows: 'ns' (p-value $\geq$ 0.05), '*' (0.01 $\leq$ p-value $<$ 0.05), '**' (0.001 $\leq$ p-value $<$ 0.01), and '***' (p-value $<$ 0.001). The text in bold denotes the best performance, while underlined signifies the second best. Gray indicates a baseline performance and red indicates a decrease in performance.

			CIFAR-100			
Layer	p_{init}	**AlexNet**	**VGG-16**	**ResNet-18**	**ResNet-34**	**ConvNeXt-T**
(Base) Conv	-	66.05 ± 0.33	70.26 ± 0.29	71.22 ± 0.18	72.47 ± 0.23	58.36 ± 6.48
(Large) Conv	-	***54.53 ± 0.65	**64.82 ± 2.92	***72.80 ± 0.27	***73.52 ± 0.11	$^{\text{ns}}$54.13 ± 1.14
$^{\dagger}L_p$-Conv	256	$^{\text{ns}}$65.95 ± 0.32	**71.03 ± 0.38	$^{\text{ns}}$71.24 ± 0.23	$^{\text{ns}}$72.61 ± 0.27	$^{\text{ns}}$60.34 ± 2.80
L_p-Conv	16	****67.12 ± 0.37**	**70.87 ± 0.23	***72.35 ± 0.30	***73.32 ± 0.23	$^{\text{ns}}$61.30 ± 1.71
L_p-Conv	8	**66.85 ± 0.18	**71.14 ± 0.29	***72.26 ± 0.28	***73.37 ± 0.15	$^{\text{ns}}$59.94 ± 5.04
L_p-Conv	4	*66.68 ± 0.28	***71.71 ± 0.36	***73.00 ± 0.15	***74.07 ± 0.22	$^{\text{ns}}$59.34 ± 7.53
L_p-Conv	2	$^{\text{ns}}$66.13 ± 0.33	*****72.88 ± 0.30**	*****73.86 ± 0.14**	*****74.95 ± 0.11**	$^{\text{ns}}$**62.61 ± 3.03**
			TinyImageNet			
Layer	p_{init}	**AlexNet**	**VGG-16**	**ResNet-18**	**ResNet-34**	**ConvNeXt-T**
(Base) Conv	-	52.25 ± 0.35	67.75 ± 0.07	66.63 ± 0.51	69.22 ± 0.11	70.25 ± 0.45
(Large) Conv	-	***35.52 ± 0.46	$^{\text{ns}}$66.96 ± 1.50	***68.33 ± 0.19	$^{\text{ns}}$69.46 ± 0.36	$^{\text{ns}}$68.66 ± 1.50
$^{\dagger}L_p$-Conv	256	$^{\text{ns}}$52.60 ± 0.12	$^{\text{ns}}$67.72 ± 0.18	$^{\text{ns}}$66.37 ± 0.55	$^{\text{ns}}$69.27 ± 0.27	$^{\text{ns}}$70.45 ± 0.44
L_p-Conv	16	***53.98 ± 0.50	***69.29 ± 0.25	**67.72 ± 0.43	**70.00 ± 0.33	$^{\text{ns}}$70.62 ± 0.30
L_p-Conv	8	**54.07 ± 0.91	***69.72 ± 0.16	*67.63 ± 0.45	***69.81 ± 0.23	$^{\text{ns}}$70.52 ± 0.36
L_p-Conv	4	*****54.30 ± 0.48**	***69.79 ± 0.30	**68.20 ± 0.50	**69.99 ± 0.44	$^{\text{ns}}$**70.74 ± 0.37**
L_p-Conv	2	***54.13 ± 0.53	*****69.96 ± 0.45**	*****68.45 ± 0.36**	*****70.43 ± 0.24**	$^{\text{ns}}$70.72 ± 0.31

Based on the observation that L_p-convolution tends to perform better as it approaches biologically observed RFs with $p_{\text{init}} = 2$, we posed the question of whether the neural representation of artificial models with biological RFs aligns more closely with the representation of VC. To address this, we compared the neural representations of TinyImageNet-trained CNNs from Table 1 by presenting the 118 Natural Scene images, with the mouse VC representations. To facilitate model comparison, we extracted the representative value, maximum SSM, chosen from pair-wise SSMs across the convolutional layers and the VC subregions (See pair-wise SSMs in Appendix A.12). In the results, models with p_{init} closer to 2 generally exhibited better alignment with the brain (Fig. 5b). In summary, we find that L_p-convolution tends to achieve better alignment with the brain as it approximates a Gaussian distribution.

7 Related Works

Resurgence of large kernels in convolution In the early stages of CNN development, large kernels were not widely adopted, with their use predominantly confined to the initial layers (Krizhevsky et al., 2012; Szegedy et al., 2015; 2017). Attempts to enlarge kernel size sometimes led to a decline in classification performance (Peng et al., 2017). Consequently, the more favored strategy was stacking smaller kernels (1x1, 3x3) (Simonyan & Zisserman, 2014; He et al., 2016).

The advent of Vision Transformers (ViTs) marked a paradigm shift from traditional CNN models, with the Swin Transformer emphasizing the significance of both attention mechanisms and large receptive fields, thereby renewing interest in large kernel CNNs (Dosovitskiy et al., 2020; Liu et al., 2021; Touvron et al., 2021; Vaswani et al., 2021; Liu et al., 2021). Recent innovations such as RepLKNet and SLaK have showcased performance comparable to ViTs, highlighting the potential of large kernel CNNs in modern computer vision (Ding et al., 2022; Liu et al., 2023). However, the effectiveness of large kernels in historically successful CNN models remains unexplored.

In this paper, we implemented large-kernel convolution by applying trainable masks to existing filters and introducing Gaussian-based structured sparsity for adjustments in receptive fields tailored to specific tasks. This methodology contrasts with recent approaches that incorporate unstructured row-rank sparsity directly into filters, which may necessitate extensive hyperparameter tuning. Our train-

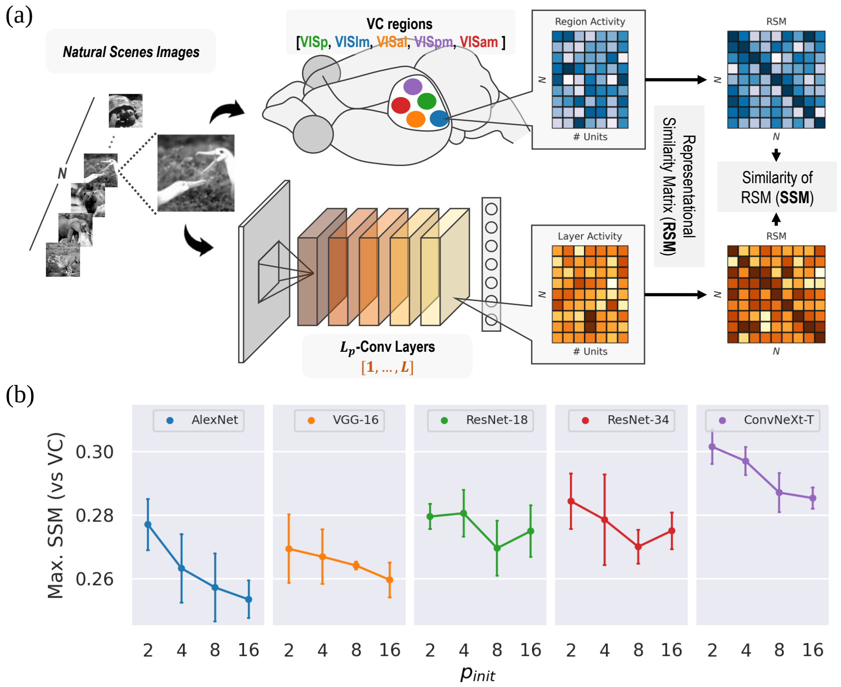

Figure 5: **Representational similarity between biological brain and artificial models using natural images** (a) Schematical illustration of representational similarity analysis from neural activities of mouse VC L2/3 subregions and convolutional layers of TinyImageNet-trained CNNs; Unit activities in both mouse brain or CNNs were obtained from N number of image inputs; $N \times N$ representational similarity matrix (RSM) was constructed for every subregions or layers by measuring the correlations across unit activities. The similarity of the RSMs (SSM) between the V1 region and CNN Conv layer was measured by calculating Kendall's rank correlation coefficient. (b) For the comparison of the representational similarity score in L_p-models, the maximum SSM score was collected as the representative value among all pair-wise SSM scores across regions and layers; the two-sample Student's t-test was conducted for statistical analysis and demonstrated statistical significance ($p_{\text{init}} = 2$ vs. others) with p-value<0.05 (*), p-value<0.01 (**), p-value<0.001 (***).

able masks streamline the optimization process by automatically adjusting key parameters, thereby facilitating the application of large kernel training in both traditional and modern CNN architectures.

Gaussian distribution as receptive field of visual information processing In biological systems, computational neuroimaging studies have uncovered that population receptive fields (pRFs) in the human visual system exhibit Gaussian distributions, shedding light on population-level insights (Wandell & Winawer, 2015). Recent research underscores the predominance of circular pRF shapes in the early visual cortex (Lerma-Usabiaga et al., 2021).

In the realm of artificial systems, the concept of effective receptive fields (ERFs) was introduced by Luo et al. (2016). Their findings indicate that ERFs in CNNs display Gaussian-like properties and are significantly smaller than their theoretical counterparts, thereby providing critical insights into how information is integrated across layers (Luo et al., 2016).

The prevailing understanding is that the Gaussian-like nature of RFs in both biological and artificial systems arises from the cumulative effect of convolutions through stacked layers. However, in our study, we show that the inherently Gaussian-like RFs — not a result of the cumulative stacking of layers —, could be beneficial in visual processing and more accurate in the explanation of the brain's neural representation.

8 Conclusion

The emergence of CNNs stands as one of the most significant events in the history of artificial intelligence (Krizhevsky et al., 2012). CNN-based models have led to the development of numerous commercial applications, generating substantial industrial value (Alzubaidi et al., 2021). Notably, CNNs have not only played a pivotal role in engineering but have also become a major model in the study of visual processing in the brain (Lindsay, 2021). However, with the recent advent of Vision Transformers, the throne of dominance as a vision model appears to be shifting away from CNNs (Dosovitskiy et al., 2020). Yet, the emergence of large-kernel CNNs has prompted a reevaluation of the potential of CNNs Ding et al. (2022); Liu et al. (2023).

In this study, we introduced a novel L_p-convolution, based on the MPND, with the objective of narrowing the gap between artificial and biological RFs, and subsequently crafting neural network modules more aligned with biological structures. Brain-inspired L_p-convolution enables the cultivation of diverse-shaped RFs with Gaussian-based structured sparsity, adaptable to various rotations, distortions, and scales, and tailored for specific tasks. Significantly, L_p-convolution showcases its adaptability and compatibility across an extensive spectrum of CNN models, from the conventional to the contemporary, underscoring its proficiency, especially in contexts involving large kernels. We believe our research serves as a noteworthy illustration of the symbiotic relationship between advancements in artificial intelligence and our understanding of neural processes.

References

Laith Alzubaidi, Jinglan Zhang, Amjad J Humaidi, Ayad Al-Dujaili, Ye Duan, Omran Al-Shamma, José Santamaría, Mohammed A Fadhel, Muthana Al-Amidie, and Laith Farhan. Review of deep learning: Concepts, cnn architectures, challenges, applications, future directions. *Journal of big Data*, 8:1–74, 2021.

Brandon Amos and J Zico Kolter. Optnet: Differentiable optimization as a layer in neural networks. In *International Conference on Machine Learning*, pp. 136–145. PMLR, 2017.

Shahab Bakhtiari, Patrick Mineault, Timothy Lillicrap, Christopher Pack, and Blake Richards. The functional specialization of visual cortex emerges from training parallel pathways with self-supervised predictive learning. *Advances in Neural Information Processing Systems*, 34:25164–25178, 2021.

Ekin Dogus Cubuk, Barret Zoph, Jon Shlens, and Q RandAugment Le. Practical automated data augmentation with a reduced search space. In *Proceedings of the IEEE/CVF Conference on Computer Vision and Pattern Recognition Workshops*, pp. 702–703.

Saskia EJ de Vries, Jerome A Lecoq, Michael A Buice, Peter A Groblewski, Gabriel K Ocker, Michael Oliver, David Feng, Nicholas Cain, Peter Ledochowitsch, Daniel Millman, et al. A large-scale standardized physiological survey reveals functional organization of the mouse visual cortex. *Nature neuroscience*, 23(1):138–151, 2020.

Barry J Devereux, Alex Clarke, Andreas Marouchos, and Lorraine K Tyler. Representational similarity analysis reveals commonalities and differences in the semantic processing of words and objects. *Journal of Neuroscience*, 33(48):18906–18916, 2013.

Jörn Diedrichsen and Nikolaus Kriegeskorte. Representational models: A common framework for understanding encoding, pattern-component, and representational-similarity analysis. *PLoS computational biology*, 13(4):e1005508, 2017.

Jörn Diedrichsen, Eva Berlot, Marieke Mur, Heiko H Schütt, Mahdiyar Shahbazi, and Nikolaus Kriegeskorte. Comparing representational geometries using whitened unbiased-distance-matrix similarity. *arXiv preprint arXiv:2007.02789*, 2020.

Xiaohan Ding, Xiangyu Zhang, Jungong Han, and Guiguang Ding. Scaling up your kernels to 31x31: Revisiting large kernel design in cnns. In *Proceedings of the IEEE/CVF conference on computer vision and pattern recognition*, pp. 11963–11975, 2022.

Alexey Dosovitskiy, Lucas Beyer, Alexander Kolesnikov, Dirk Weissenborn, Xiaohua Zhai, Thomas Unterthiner, Mostafa Dehghani, Matthias Minderer, Georg Heigold, Sylvain Gelly, et al. An image is worth 16x16 words: Transformers for image recognition at scale. In *International Conference on Learning Representations*, 2020.

Kunihiko Fukushima. Neocognitron: A self-organizing neural network model for a mechanism of pattern recognition unaffected by shift in position. *Biological cybernetics*, 36(4):193–202, 1980.

Irwin R Goodman and Samuel Kotz. Multivariate θ-generalized normal distributions. *Journal of Multivariate Analysis*, 3(2):204–219, 1973.

Kaiming He, Xiangyu Zhang, Shaoqing Ren, and Jian Sun. Deep residual learning for image recognition. In *Proceedings of the IEEE conference on computer vision and pattern recognition*, pp. 770–778, 2016.

Gao Huang, Yu Sun, Zhuang Liu, Daniel Sedra, and Kilian Q Weinberger. Deep networks with stochastic depth. In *Computer Vision–ECCV 2016: 14th European Conference, Amsterdam, The Netherlands, October 11–14, 2016, Proceedings, Part IV 14*, pp. 646–661. Springer, 2016.

Gao Huang, Zhuang Liu, Laurens Van Der Maaten, and Kilian Q Weinberger. Densely connected convolutional networks. In *Proceedings of the IEEE conference on computer vision and pattern recognition*, pp. 4700–4708, 2017.

David H Hubel and Torsten N Wiesel. Receptive fields, binocular interaction and functional architecture in the cat's visual cortex. *The Journal of physiology*, 160(1):106, 1962.

David H Hubel and Torsten N Wiesel. Receptive fields and functional architecture in two nonstriate visual areas (18 and 19) of the cat. *Journal of neurophysiology*, 28(2):229–289, 1965.

Seyed-Mahdi Khaligh-Razavi and Nikolaus Kriegeskorte. Deep supervised, but not unsupervised, models may explain it cortical representation. *PLoS computational biology*, 10(11):e1003915, 2014.

Alex Krizhevsky, Geoffrey Hinton, et al. Learning multiple layers of features from tiny images. 2009.

Alex Krizhevsky, Ilya Sutskever, and Geoffrey E Hinton. Imagenet classification with deep convolutional neural networks. *Advances in neural information processing systems*, 25, 2012.

Quoc Le and Tomas Mikolov. Distributed representations of sentences and documents. In *International conference on machine learning*, pp. 1188–1196. PMLR, 2014.

Yann LeCun, Bernhard Boser, John S Denker, Donnie Henderson, Richard E Howard, Wayne Hubbard, and Lawrence D Jackel. Backpropagation applied to handwritten zip code recognition. *Neural computation*, 1(4):541–551, 1989.

Garikoitz Lerma-Usabiaga, Jonathan Winawer, and Brian A Wandell. Population receptive field shapes in early visual cortex are nearly circular. *Journal of Neuroscience*, 41(11):2420–2427, 2021.

Grace W Lindsay. Convolutional neural networks as a model of the visual system: Past, present, and future. *Journal of cognitive neuroscience*, 33(10):2017–2031, 2021.

Tianlong Liu, Shiwei andrs Chen, Xiaohan Chen, Xuxi Chen, Qiao Xiao, Boqian Wu, Tommi Kärkkainen, Mykola Pechenizkiy, Decebal C Mocanu, and Zhangyang Wang. More convnets in the 2020s: Scaling up kernels beyond 51x51 using sparsity. In *International Conference on Learning Representations, ICLR 2023*, 2023.

Ze Liu, Yutong Lin, Yue Cao, Han Hu, Yixuan Wei, Zheng Zhang, Stephen Lin, and Baining Guo. Swin transformer: Hierarchical vision transformer using shifted windows. In *Proceedings of the IEEE/CVF international conference on computer vision*, pp. 10012–10022, 2021.

Zhuang Liu, Hanzi Mao, Chao-Yuan Wu, Christoph Feichtenhofer, Trevor Darrell, and Saining Xie. A convnet for the 2020s. In *Proceedings of the IEEE/CVF conference on computer vision and pattern recognition*, pp. 11976–11986, 2022.

Ilya Loshchilov and Frank Hutter. Decoupled weight decay regularization. *arXiv preprint arXiv:1711.05101*, 2017.

Wenjie Luo, Yujia Li, Raquel Urtasun, and Richard Zemel. Understanding the effective receptive field in deep convolutional neural networks. *Advances in neural information processing systems*, 29, 2016.

David Martin, Charless Fowlkes, Doron Tal, and Jitendra Malik. A database of human segmented natural images and its application to evaluating segmentation algorithms and measuring ecological statistics. In *Proceedings Eighth IEEE International Conference on Computer Vision. ICCV 2001*, volume 2, pp. 416–423. IEEE, 2001.

Johannes Mehrer, Courtney J Spoerer, Nikolaus Kriegeskorte, and Tim C Kietzmann. Individual differences among deep neural network models. *Nature communications*, 11(1):5725, 2020.

Thao Nguyen, Maithra Raghu, and Simon Kornblith. Do wide and deep networks learn the same things? uncovering how neural network representations vary with width and depth. *arXiv preprint arXiv:2010.15327*, 2020.

Chingis Oinar. How to solve sudoku with convolutional neural networks (cnn). `https://github.com/chingisooinar/sudoku-solver.pytorch`, 2021.

Adriana Olmos and Frederick AA Kingdom. A biologically inspired algorithm for the recovery of shading and reflectance images. *Perception*, 33(12):1463–1473, 2004.

Rasmus Palm, Ulrich Paquet, and Ole Winther. Recurrent relational networks. *Advances in neural information processing systems*, 31, 2018.

Kyubyong Park. Can convolutional neural networks crack sudoku puzzles? `https://github.com/Kyubyong/sudoku`, 2018.

Adam Paszke, Sam Gross, Francisco Massa, Adam Lerer, James Bradbury, Gregory Chanan, Trevor Killeen, Zeming Lin, Natalia Gimelshein, Luca Antiga, et al. Pytorch: An imperative style, high-performance deep learning library. *Advances in neural information processing systems*, 32, 2019.

Chao Peng, Xiangyu Zhang, Gang Yu, Guiming Luo, and Jian Sun. Large kernel matters–improve semantic segmentation by global convolutional network. In *Proceedings of the IEEE conference on computer vision and pattern recognition*, pp. 4353–4361, 2017.

L Federico Rossi, Kenneth D Harris, and Matteo Carandini. Spatial connectivity matches direction selectivity in visual cortex. *Nature*, 588(7839):648–652, 2020.

David E Rumelhart, Geoffrey E Hinton, and Ronald J Williams. Learning representations by back-propagating errors. *nature*, 323(6088):533–536, 1986.

Jianghong Shi, Eric Shea-Brown, and Michael Buice. Comparison against task driven artificial neural networks reveals functional properties in mouse visual cortex. *Advances in Neural Information Processing Systems*, 32, 2019.

Karen Simonyan and Andrew Zisserman. Very deep convolutional networks for large-scale image recognition. *arXiv preprint arXiv:1409.1556*, 2014.

Christian Szegedy, Wei Liu, Yangqing Jia, Pierre Sermanet, Scott Reed, Dragomir Anguelov, Dumitru Erhan, Vincent Vanhoucke, and Andrew Rabinovich. Going deeper with convolutions. In *Proceedings of the IEEE conference on computer vision and pattern recognition*, pp. 1–9, 2015.

Christian Szegedy, Sergey Ioffe, Vincent Vanhoucke, and Alexander Alemi. Inception-v4, inception-resnet and the impact of residual connections on learning. In *Proceedings of the AAAI conference on artificial intelligence*, volume 31, 2017.

Hugo Touvron, Matthieu Cord, Matthijs Douze, Francisco Massa, Alexandre Sablayrolles, and Hervé Jégou. Training data-efficient image transformers & distillation through attention. In *International conference on machine learning*, pp. 10347–10357. PMLR, 2021.

J Hans Van Hateren and Arjen van der Schaaf. Independent component filters of natural images compared with simple cells in primary visual cortex. *Proceedings of the Royal Society of London. Series B: Biological Sciences*, 265(1394):359–366, 1998.

Ashish Vaswani, Prajit Ramachandran, Aravind Srinivas, Niki Parmar, Blake Hechtman, and Jonathon Shlens. Scaling local self-attention for parameter efficient visual backbones. In *Proceedings of the IEEE/CVF Conference on Computer Vision and Pattern Recognition*, pp. 12894–12904, 2021.

Brian A Wandell and Jonathan Winawer. Computational neuroimaging and population receptive fields. *Trends in cognitive sciences*, 19(6):349–357, 2015.

Po-Wei Wang, Priya Donti, Bryan Wilder, and Zico Kolter. Satnet: Bridging deep learning and logical reasoning using a differentiable satisfiability solver. In *International Conference on Machine Learning*, pp. 6545–6554. PMLR, 2019.

Paul Werbos. Beyond regression: New tools for prediction and analysis in the behavioral sciences. *PhD thesis, Committee on Applied Mathematics, Harvard University, Cambridge, MA*, 1974.

Ross Wightman. Pytorch image models. `https://github.com/rwightman/`, 2019.

Sanghyun Woo, Shoubhik Debnath, Ronghang Hu, Xinlei Chen, Zhuang Liu, In So Kweon, and Saining Xie. Convnext v2: Co-designing and scaling convnets with masked autoencoders. In *Proceedings of the IEEE/CVF Conference on Computer Vision and Pattern Recognition*, pp. 16133–16142, 2023.

Saining Xie, Ross Girshick, Piotr Dollár, Zhuowen Tu, and Kaiming He. Aggregated residual transformations for deep neural networks. In *Proceedings of the IEEE conference on computer vision and pattern recognition*, pp. 1492–1500, 2017.

Sangdoo Yun, Dongyoon Han, Seong Joon Oh, Sanghyuk Chun, Junsuk Choe, and Youngjoon Yoo. Cutmix: Regularization strategy to train strong classifiers with localizable features. In *Proceedings of the IEEE/CVF international conference on computer vision*, pp. 6023–6032, 2019.

Hongyi Zhang, Moustapha Cisse, Yann N Dauphin, and David Lopez-Paz. mixup: Beyond empirical risk minimization. *arXiv preprint arXiv:1710.09412*, 2017.

Zhun Zhong, Liang Zheng, Guoliang Kang, Shaozi Li, and Yi Yang. Random erasing data augmentation. In *Proceedings of the AAAI conference on artificial intelligence*, volume 34, pp. 13001–13008, 2020.

A Appendix

A.1 Biological RFs

For the biological RF analysis, we have analyzed *in vivo* intracortical connectivity dataset of Rossi et al. (2020) collected from the mouse primary visual cortex (V1) (Fig. 1a). It contains both excitatory (CaMK2a-positive) and inhibitory (Gad2-positive) layer 2/3 neuronal spatial connectivity distribution (Fig. 1b) which was determined by recording GCaMP6 signals (calcium activities) of pre-and post-synaptic pairs (Fig. 7 and 6).

Given a post-synaptic neuron positioned at (x_0, y_0), (Fig. 1b black), and the N_b number of functional synapse positions $x_n, y_n \in (-\infty, \infty)$ for $n = 1, 2, ..., N_b$, then relative offsets are defined as $(\Delta x_n, \Delta y_n) = (x_n - x_0, y_n - y_0)$. We summarize functional synapse positions for biological RF as following

$$\Delta \mathbf{s}_{\text{b}} = [(\Delta x_n, \Delta y_n)]_{n=1}^{N_b}. \tag{5}$$

A.2 Artificial RFs

For the artificial RF analysis, we used untrained or pre-trained AlexNet[4] with inputs (224 × 224) of 17 images either generated from Gaussian noises or selected among 118 Natural Scenes images datasets (See details in Appendix A.10 and Fig. 7). When image inputs were shown to AlexNet, we extracted RFs of the functional synapse from the first convolutional layer (Conv1) (Fig. 1, c and d).

Given the input $\mathcal{X} \in \mathbb{R}^{C_i \times H \times W}$ and weights parameters for Artificial RFs $\mathcal{W}_{\text{ARF}} \in \mathbb{R}^{C_i \times K_h \times K_w}$, the post-synaptic unit in the Convolution layer, receives weighted-input $\mathcal{Z} \in \mathbb{R}^{V \times C_i \times K_h \times K_w}$, the results of element-wise multiplication between partial input and filters, where $\mathcal{Z}_{v=m*(H-K_h+1)+n} = \mathcal{X}_{\cdot,m:m+K_h-1,n:n+K_w-1} \odot \mathcal{W}$ (Fig. 1d black) for $0 \leq m \leq H - K_h$ and $\leq n \leq W - K_w$. We calculate the weighted input as the convolution operation without summation across width, height and input channel. As a result, weighted input $\mathcal{Z}$ has $V \times C_i \times K_h \times K_w$ shape, where $V = (H - K_h + 1) \times (W - K_w + 1)$, and $\mathcal{Z}_v \in \mathbb{R}^{C_i \times K_h \times K_w}$ denotes the v-th element of $\mathcal{Z}$. Here, C_i, H, W, K_h and K_w denote the number of input channels, input height, input width, kernel height and kernel width, respectively. For simplicity, we assume that there is stride one and no zero-padding. For $h \in [0, \cdots, K_h - 1]$ and $w \in [0, \cdots, K_w - 1]$, the relative offsets from the kernel center are defined as follows

$$\Delta s = (\Delta h, \Delta w) = (h - \frac{K_h}{2}, w - \frac{K_w}{2}). \tag{6}$$

Since spatial connectivity pattern in the biological synapse is measured by the functional calcium activities and given as coordinates, we applied a similar approach to that of CNN layers. We collected N_a functional weighted-inputs (functional synapses) where N_a represents the number of cases where each elements of $|\mathcal{Z}|$ exceeds a threshold θ. Here, we defined θ as the standard deviation of $|\mathcal{Z}|$ [5]. This selection process yielded a different set of functional synapses input-dependent manner. We summarize functional synapse positions for artificial RF as following

$$\Delta \mathbf{s}_{\text{a}} = \{(v, k, \Delta h, \Delta w) | \mathcal{Z}_{v,k,h,w} > \theta\}, \text{ where } |\Delta \mathbf{s}_{\text{a}}| = N_a. \tag{7}$$

[4] For the pre-trained model, we used the torchvision's ImageNet-1k pre-trained model

[5] We determined the activity threshold based on a common method used in neuroscience to extract meaningful patterns in neural activity, which is similar to calculating the Z-score and typically setting a threshold at a range of 2 to 3 standard deviations to identify values that are statistically significant.

A.3 Gaussian distributed functional synapses of post-synaptic neuron in mouse V1 layer 2/3

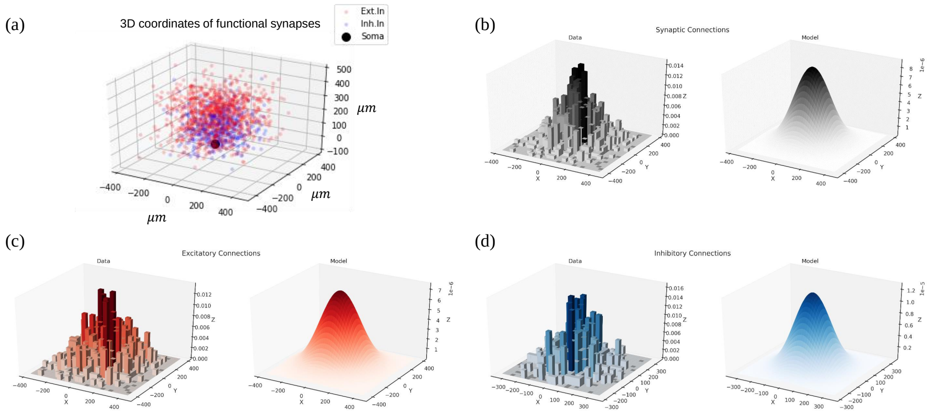

Figure 6: **Distribution of post-synaptic functional synapses in mouse V1 layer 2/3** (a) Using dataset from Rossi et al. (2020), 3D scatter plot represent relative positions of both excitatory (red) and inhibitory (blue) functional synapses from the soma of the post-synaptic neuron. (b-d) 2d histogram (left) and Gaussian fitted probability density function (right), showing the laminar organization of functional synapses for all (b), excitatory (c), and inhibitory (d)

A.4 Individual receptive fields collected from both biological and artificial systems

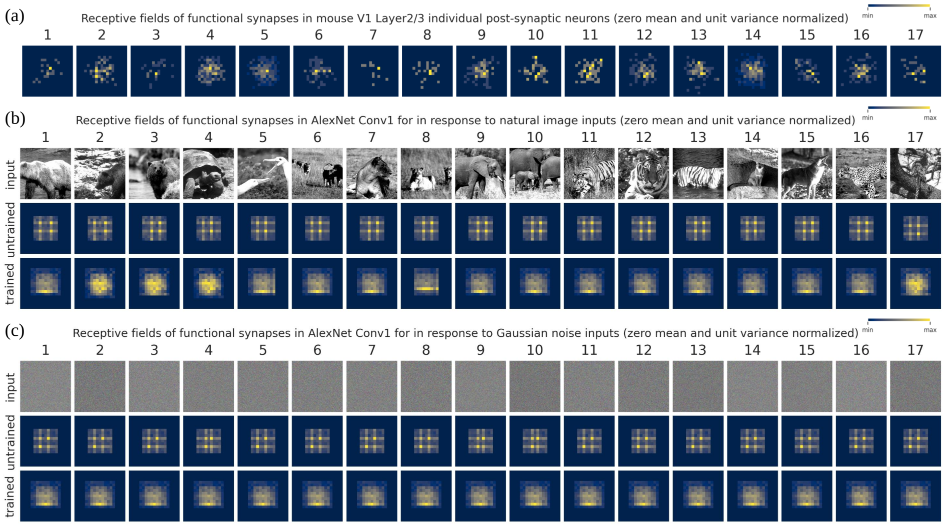

Figure 7: **Biological and artificial receptive fields with visual stimulus** The receptive field discussed in this figure specifically refers to the spatial connectivity patterns of synapses. Note that this differs from receptive fields typically associated with low-level visual feature selectivity. (a) Receptive fields of individual neurons in V1 Layer2/3 from the dataset Rossi et al. (2020) (b) Receptive fields of untrained or ImageNet-1k pretrained AlexNet's Conv1 layer when Natural Scenes images were shown (c) Receptive fields of untrained or ImageNet-1k pretrained AlexNet's Conv1 layer when Gaussian RGB noise were shown. All receptive fields are zero mean unit variance normalized.

A.5 Experimental details for Sudoku Challenge

We utilized the extensive 1M-sudoku dataset (Park, 2018), a resource also utilized in prior works (Amos & Kolter, 2017; Palm et al., 2018; Wang et al., 2019). Sudoku, a widely popular number puzzle, involves organizing digits in a grid such that each row (1×9), column (9×1), and box (3×3) contains all numbers from 1 to 9. In the Sudoku challenge, where achieving these three objectives simultaneously is essential for complete Sudoku solving, there is an advantage that we can test the applicability and effectiveness of evolving RFs in the L_p-convolution. To achieve this, we compared five distinct models of Sudoku CNN: (3×3) Base model, (7×7) Large model, (7×7) $L_p(p_{\text{init}} = 2)$, (7×7) $L_p(p_{\text{init}} = 16)$, and finally (7×7) $L_p^{\dagger}(p_{\text{init}} = 256)$ (frozen p and $\mathbf{C}$ model) 2. For numerical stability, we clipped $p \geq 2$ during the training of the Sudoku-solving task. The inputs, targets, and model architecture are outlined in Figure 4a. As illustrated, our model comprises repeated Conv2dSame blocks, originally introduced in SudokuCNN (Oinar, 2021). Each Conv2dSame block encompasses Reflection padding, followed by a conventional Convolutional or L_p-Convolutional layer, Batch Normalization, and an activation function. The Convolutional layer has 256 channels, and the number of blocks is set at $L = 10$.

A.6 Conformational analysis of L_p-masks

We defined the properties of scale (α), rotation (θ), and distortion (γ) through Singular Value Decomposition (SVD) on $\mathbf{C}$, covariance matrix for each output channel, as shown in the following equation:

$$\mathbf{C} = \mathbf{U}\mathbf{\Lambda}\mathbf{V}^T. \tag{8}$$

Here, $\mathbf{U}$ and $\mathbf{V}$ represent 2×2 unitary matrices containing the left and right singular vectors. $\mathbf{\Lambda}$ is a diagonal matrix containing the singular values (λ_0, λ_1). Rotation is quantified as $\theta = \arctan\left(\frac{\sin(\mathbf{V}^T[1])}{\cos(\mathbf{V}^T[1])}\right)$ (in degrees), providing a measure of rotational transformation. Distortion is quantified as $\gamma = \frac{\lambda_0}{\lambda_1}$, offering valuable information about the deformation present in the data. Scale is quantified as $\alpha = \sqrt{\left(\frac{1}{\lambda_0}\right)^2 + \left(\frac{1}{\lambda_1}\right)^2}$, indicating the size of mask. In Figure 4a, we show the example shapes of L_p-masks by reverse calculating $\mathbf{C}$ from the given α, θ, γ.

A.7 LAYER-WISE VISUALIZATION OF L_p-MASKS FOR SUDOKU-L_pCONVNET

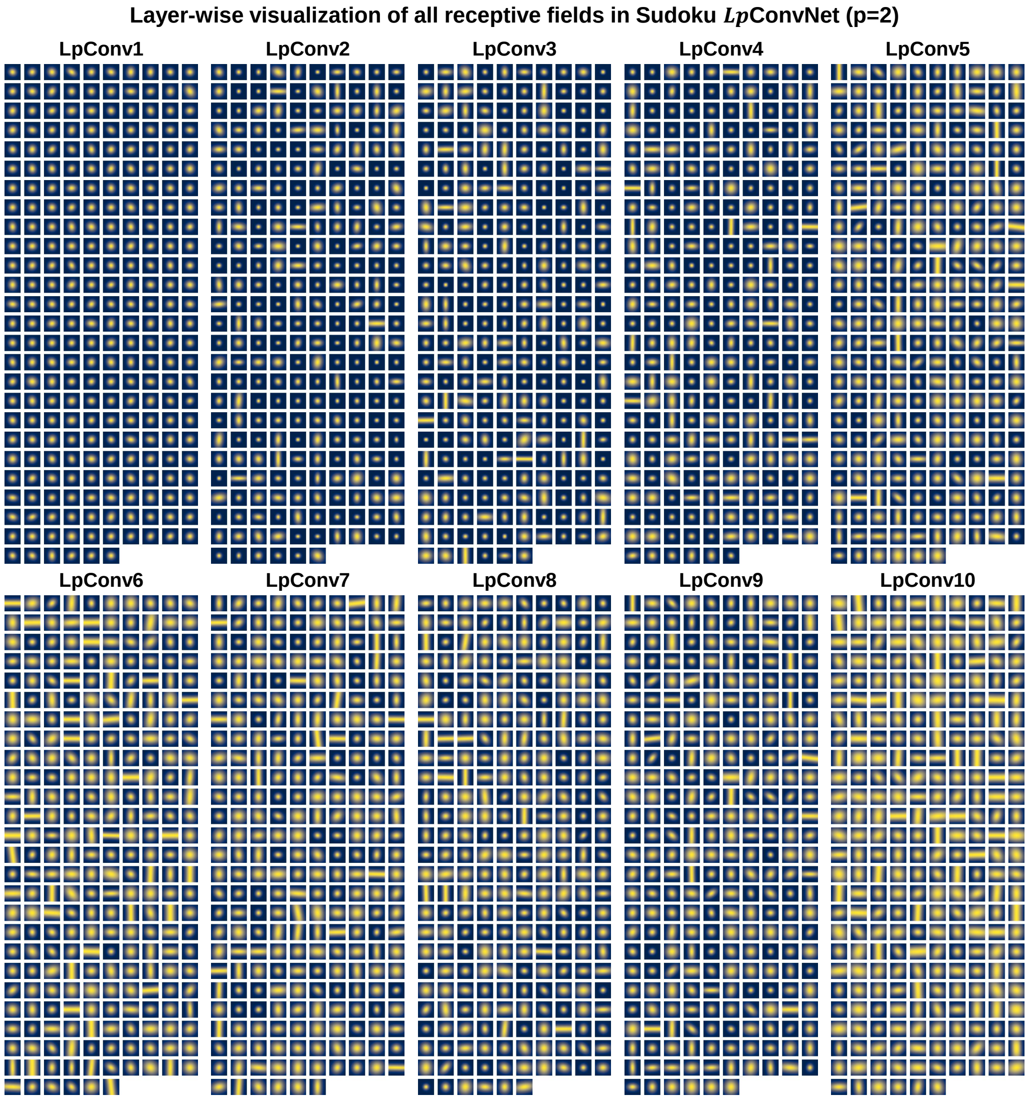

Figure 8: **Layer-wise visualization of L_p-masks for Sudoku-$L_p$convNet** All learned L_p-masks after Sudoku task training of L_p-ConvNet($p_{\text{init}} = 2$). With an increase in layer depth, the sizes of masks get larger.

A.8 Accuracy curves for Sudoku ablation experiments on L_p(p=2)

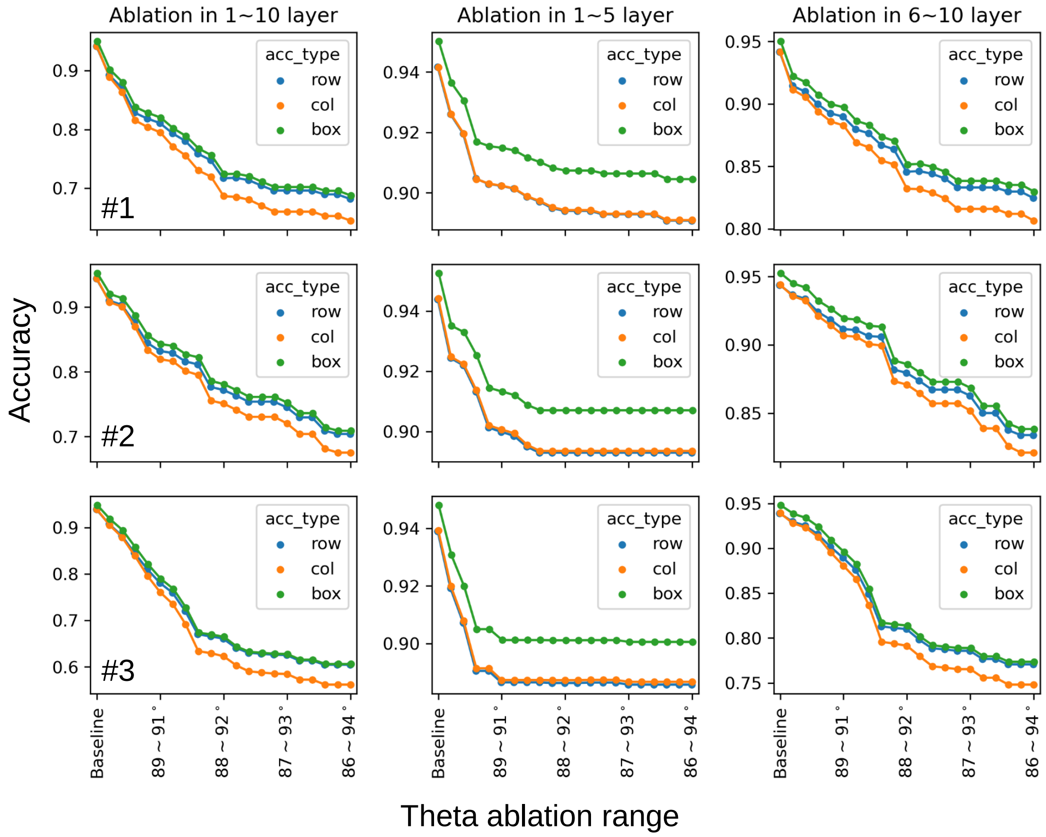

Figure 9: **Accuracy curves for Sudoku ablation experiments on L_p(p=2).** 3 individual experiments (rows) of vertical L_p-masks ablations with 3 different conditions (columns; layer 1 to 10, left; layer 1 to 5, middle; layer 6 to 10, right) on L_p(p=2)

A.9 Experimental details of vision classification task

We conducted our training on two datasets: CIFAR-100 (Krizhevsky et al., 2009) and TinyImageNet (Le & Mikolov, 2014). CIFAR-100 comprises 32×32 pixel images distributed across 100 classes, while TinyImageNet consists of 224×224 pixel images spanning 200 categories. Following standard procedures, we reported top-1 accuracy with corresponding mean and standard deviation. Our implementation is based on the **PyTorch** framework (Paszke et al., 2019), making extensive use of the **timm** repository (Wightman, 2019). We adopted a training strategy rooted in DeiT (Touvron et al., 2021), incorporating techniques such as RandAugment (Cubuk et al.), Mixup (Zhang et al., 2017), Cutmix (Yun et al., 2019), random erasing (Zhong et al., 2020), and stochastic depth (Huang et al., 2016). The optimization process employed AdamW (Loshchilov & Hutter, 2017) with a default momentum value of 0.9 and a weight decay set at 5×10^{-2}. We initialized our learning rate at 1×10^{-3} and implemented a cosine learning rate schedule. All models underwent training for 300 epochs, utilizing a batch size of 128. For CIFAR-100, training was conducted on 2 GTX 1080ti GPUs, while 2 Tesla V100 GPUs were used for TinyImageNet.

A.10 The Allen Brain Observatory dataset

The Allen Brain Observatory dataset (de Vries et al., 2020) constitutes a comprehensive standardized in vivo examination of physiological activity within the mouse visual cortex. It encompasses recordings of visually-induced calcium responses from neurons expressing GCaMP6f. This dataset encompasses cortical activity from nearly 60,000 neurons originating from six distinct visual areas, four layers, and twelve transgenic mouse Cre lines. These recordings were gathered from 243 adult mice in reaction to a diverse set of visual stimuli. In this study, we focused on utilizing the collective neural responses from five visual areas (VISal, VISam, VISl, VISp, VISpm), Layer 2/3 (depth range of 175mm to 275mm), and three mouse lines (Cux2-CreERT, Emx1-IRES-Cre, Slc17a7-IRES2-Cre) when presenting a dataset of natural scenes to the mice. This dataset comprised 118 natural images obtained from three different databases (Berkeley Segmentation Dataset (Martin et al., 2001), van Hateren Natural Image Dataset (Van Hateren & van der Schaaf, 1998), and McGill Calibrated Colour Image Database (Olmos & Kingdom, 2004)). Further details regarding the experiment can be found in (de Vries et al., 2020). In our study, we employed both images and neural responses for experiments involving representational similarity analysis to evaluate the correspondence between CNNs and the visual cortex, mirroring earlier investigations (Shi et al., 2019; Bakhtiari et al., 2021).

A.11 Representation similarity analysis

While the details of RSA are expertly addressed in Diedrichsen & Kriegeskorte (2017), let us briefly cover our specific approach. We leveraged the codebase provided by Bakhtiari et al. (2021). In RSA, we generate response matrices ($\mathbf{R}$) for brain regions and neural network layers, with dimensions $N \times M$ (where N is the number of image inputs and M is the neuron count). Using Pearson correlation, we compute similarities within matrix $\mathbf{R}$ to construct the $N \times N$ Representation Similarity Matrix (RSM). Additionally, following the methodology of Bakhtiari et al. (2021), we applied noise correction by normalizing the RSAs using the noise ceiling values. These values were obtained through comparisons of representations across different mice. For example, the noise ceiling value for VISp is derived by calculating the RSMs of VISp from different animals and taking their median. To assess the similarity between RSMs (SSM), we employ Kendall's τ for robust agreement, which helps mitigate potential bias from measurement noise Diedrichsen et al. (2020).

A.12 Pair-wise representation similarity analysis between all CNN layers and V1 subregions

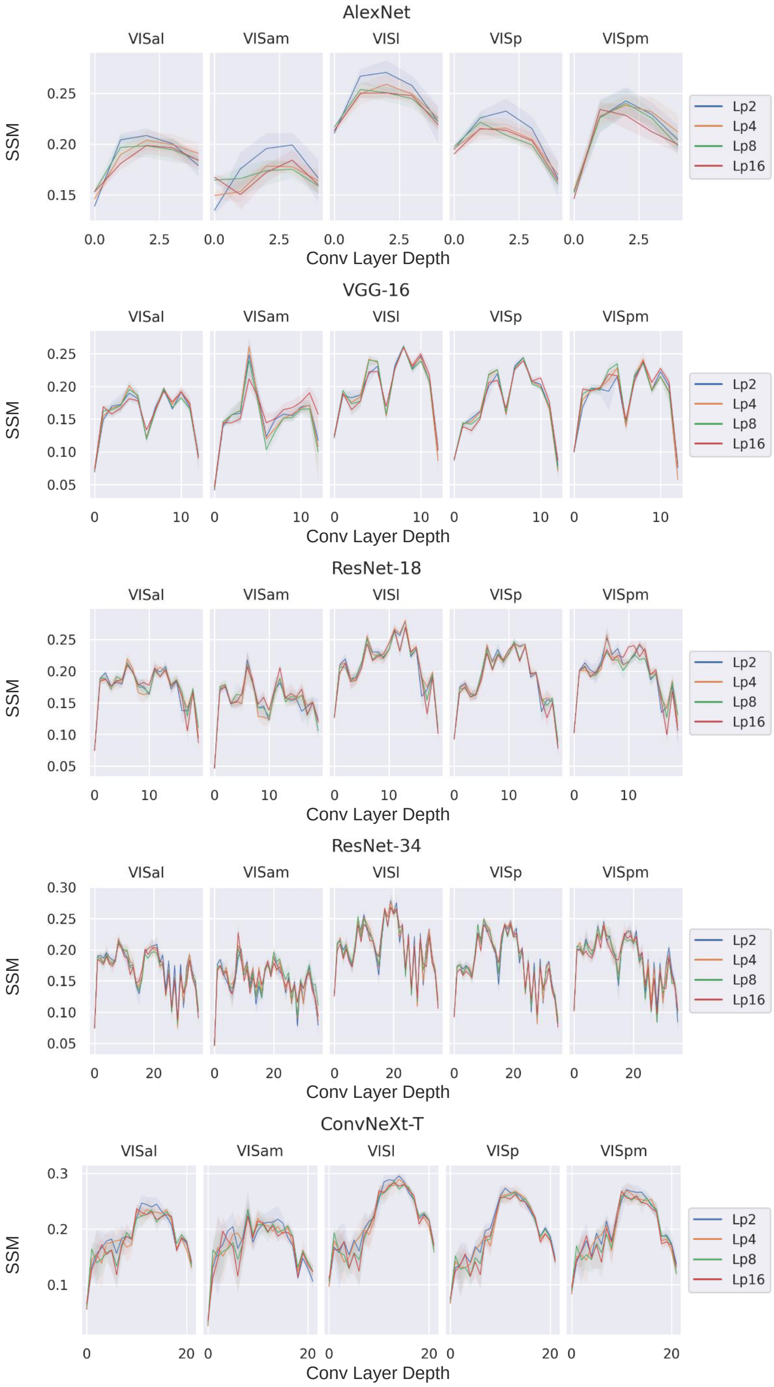

Figure 10: **Pair-wise representation similarity analysis between all CNN layers and VC subregions**. We show the SSM scores for all pairs of Conv layers from CNNs and VC subregions. y-axis, SSM score; x-axis, Conv layer depth. For Max. SSM, we choose the highest SSM among all pair-wise SSMs.

A.13 PyTorch-style pseudocode for L_p-Convolution

Algorithm 1: PyTorch-style pseudocode for L_p-Convolution

```
import torch
import torch.nn as nn
import torch.nn.functional as F

from torchvision.models import alexnet

class LpConv2d(nn.Conv2d):
   def __init__(self, p_init, sigma_init, in_channels,
                out_channels, kernel_size, stride,
                padding, **kwargs):

      ...

      # Create parameters p & C
      params_p = torch.ones( out_channels ) * p_init
      params_C = torch.zeros( out_channels, 2, 2 ) )
      params_C[:,0,0] = 1/sigma_init
      params_C[:,1,1] = 1/sigma_init

      self.p = nn.Parameter( params_p )
      self.C = nn.Parameter( params_C )

   def forward(self, input):
      # Create channel-wise lp_masks from parameters p and C
      lp_masks = get_channel_wise_lp_masks(self.p, self.C)

      # Overlay lp_masks on weight
      masked_weight = weight * lp_masks
      return F.conv2d(inputs, masked_weight, bias,
                      kernel_size, stride, padding, **kwargs)

def LpConvert(model, p_init):
   # Convert all nn.Conv2d layers into LpConv2d
   for i in range(num_layers):
      layer = model.layers[i]
      if layer is nn.Conv2d:
         model.layers[i] = LpConv2d(p_init, sigma_init, **kwargs)
   return model

# LpConvert on Alexnet for TinyImageNet
base_model = alexnet(num_classes=200)
lp2_model = LpConvert(base_model, p_init=2)
```

A.14 Visualization of functional receptive fields of pre-trained AlexNet

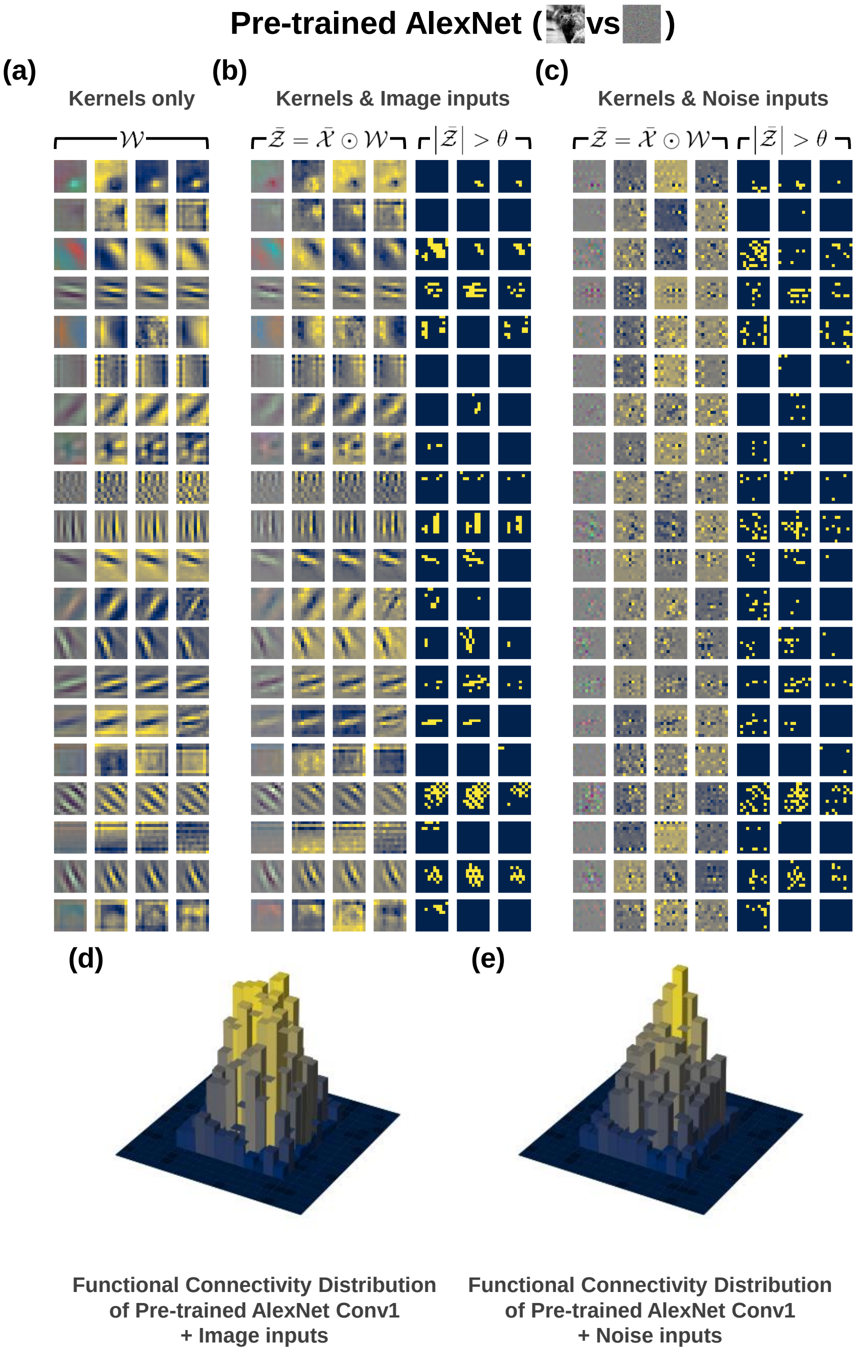

Figure 11: **Visualization of functional receptive fields of pre-trained AlexNet Conv1 with image or noise inputs**. Visualization of first 20 kernels of total 64 without inputs (a; column orders: RGB, R, G, B), with image inputs (b; column orders: RGB, R, G, B, R, G, B) with noise inputs (c; column orders: RGB, R, G, B, R, G, B). (d) Histogram of functional connectivity from (b). (e) Histogram of functional connectivity from (c). $\mathcal{W}$, Weight; $\bar{\mathcal{X}}$, kernel-sized input; $\bar{\mathcal{Z}}$, kernel-sized output; θ, activity threshold; $\odot$, element-wise product. See Appendix A.2. for methodological details.

A.15 Visualization of functional receptive fields of untrained AlexNet

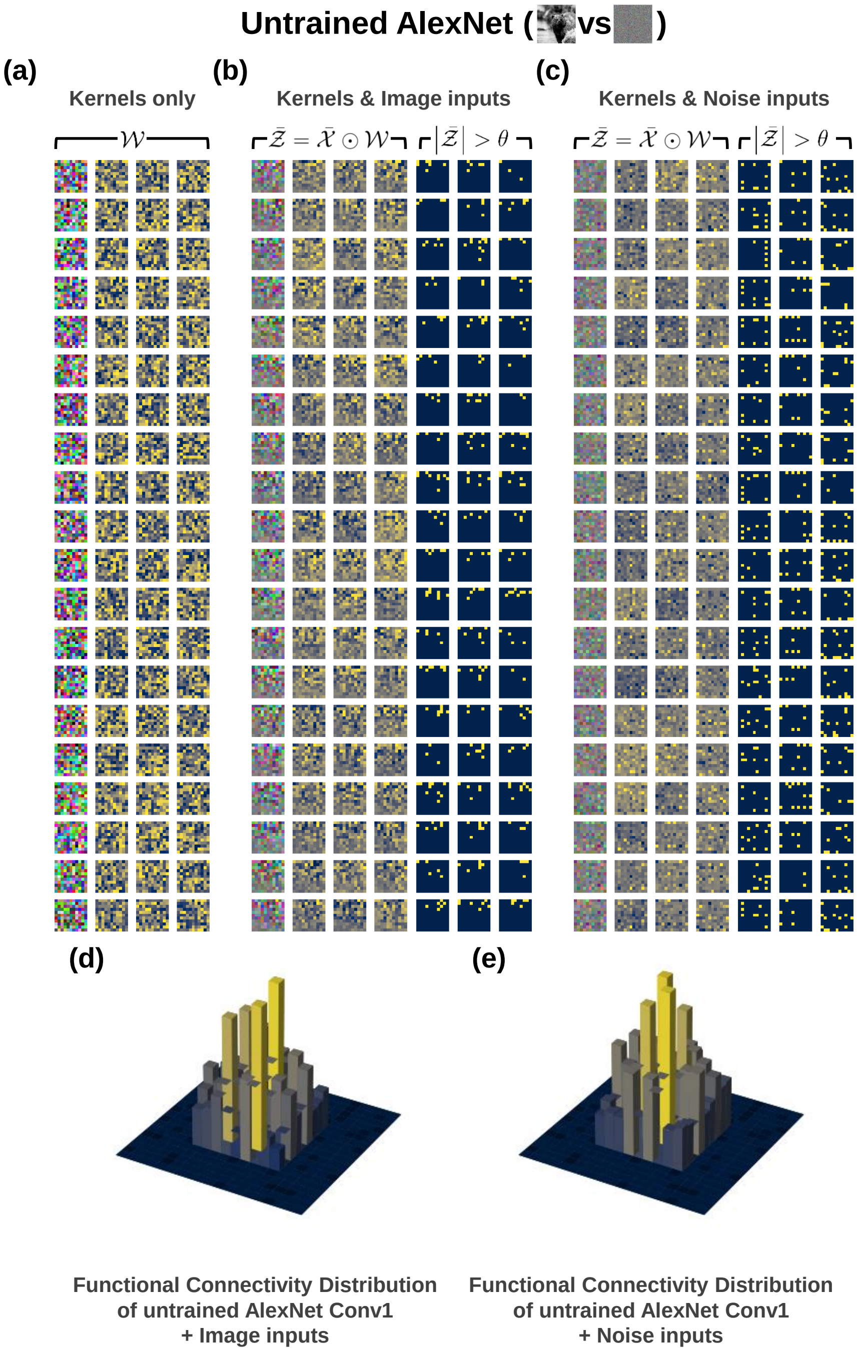

Figure 12: **Visualization of functional receptive fields of untrained AlexNet Conv1 with image or noise inputs**. Visualization of first 20 kernels of total 64 without inputs (a; column orders: RGB, R, G, B), with image inputs (b; column orders: RGB, R, G, B, R, G, B) with noise inputs (c; column orders: RGB, R, G, B, R, G, B). (d) Histogram of functional connectivity from (b). (e) Histogram of functional connectivity from (c). $\mathcal{W}$, Weight; $\bar{\mathcal{X}}$, kernel-sized input; $\bar{\mathcal{Z}}$, kernel-sized output; θ, activity threshold; $\odot$, element-wise product. See Appendix A.2. for methodological details.

A.16 VISUALIZATION OF MPND WHEN $p < 2$

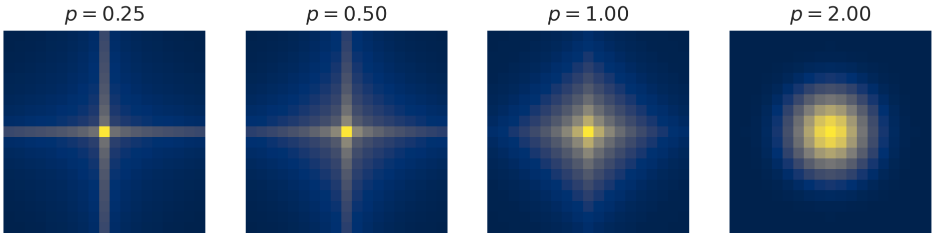

Figure 13: **Visualization of MPND when $p < 2$** Given the value of $p = 1$, MPND distribution becomes diamond shape. When $p < 1$, the distribution becomes a cross-like shape.

A.17 POST-TRAINED p-DISTRIBUTION IN L_p-MASKS

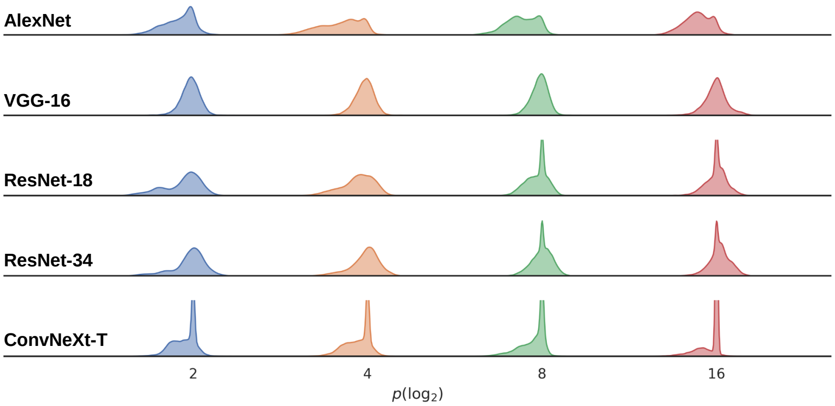

Figure 14: **CIFAR-100-trained p-distribution of L_p-masks**

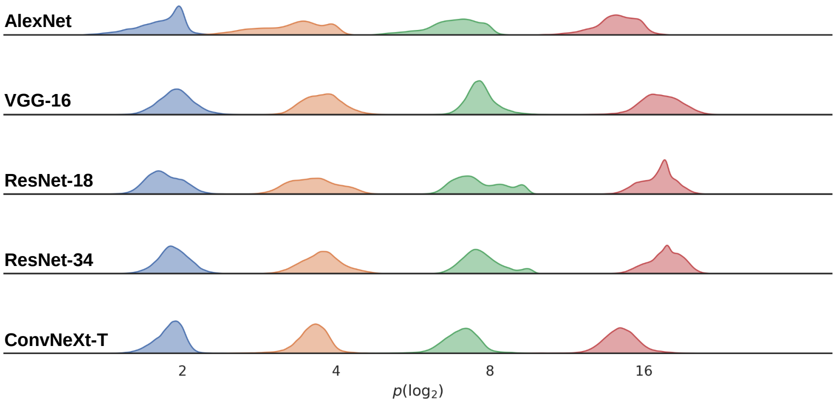

Figure 15: **TinyImageNet-trained p-distribution of L_p-masks**

Table 2: **Layer-wise p-distribution of CIFAR-100-trained L_p-masks** All values (Median ± Stdev) are calculated with p of all L_p-masks in each layer, from 5 different trials of CIFAR-100-trained models.

CIFAR-100

Model	Layer	L_p-Conv (p=2)	L_p-Conv (p=4)	L_p-Conv (p=8)	L_p-Conv (p=16)
AlexNet	1	1.99 ± 0.08	3.88 ± 0.16	7.75 ± 0.35	15.45 ± 0.68
	2	2.00 ± 0.06	3.93 ± 0.19	7.67 ± 0.52	15.35 ± 0.96
	3	1.91 ± 0.07	3.70 ± 0.16	7.64 ± 0.37	15.06 ± 0.79
	4	1.80 ± 0.13	3.38 ± 0.32	7.18 ± 0.36	14.73 ± 0.64
	5	1.82 ± 0.11	3.35 ± 0.29	7.11 ± 0.38	14.45 ± 0.68
ResNet-18	1	1.98 ± 0.11	3.85 ± 0.23	7.70 ± 0.49	15.39 ± 1.27
	2	2.01 ± 0.06	3.87 ± 0.13	7.91 ± 0.32	15.37 ± 0.84
	3	1.93 ± 0.05	3.68 ± 0.11	7.45 ± 0.25	15.30 ± 0.58
	4	1.95 ± 0.05	3.72 ± 0.12	7.61 ± 0.26	15.43 ± 0.61
	5	1.92 ± 0.05	3.65 ± 0.12	7.45 ± 0.23	15.55 ± 0.52
	6	1.98 ± 0.05	3.80 ± 0.10	7.58 ± 0.20	16.08 ± 0.56
	7	1.82 ± 0.05	3.45 ± 0.13	7.30 ± 0.26	14.92 ± 0.57
	8	1.71 ± 0.06	3.57 ± 0.17	8.00 ± 0.01	16.00 ± 0.00
	9	1.88 ± 0.05	3.61 ± 0.12	7.49 ± 0.21	15.47 ± 0.58
	10	1.93 ± 0.05	3.70 ± 0.11	7.50 ± 0.22	15.82 ± 0.48
	11	2.01 ± 0.06	3.90 ± 0.13	7.68 ± 0.21	16.28 ± 0.56
	12	1.79 ± 0.06	3.52 ± 0.13	7.35 ± 0.20	15.31 ± 0.51
	13	1.62 ± 0.05	3.42 ± 0.14	8.00 ± 0.01	16.00 ± 0.00
	14	1.93 ± 0.06	3.82 ± 0.11	7.72 ± 0.20	16.22 ± 0.56
	15	2.01 ± 0.05	3.96 ± 0.10	7.93 ± 0.20	16.54 ± 0.54
	16	2.09 ± 0.06	4.16 ± 0.11	8.07 ± 0.21	16.80 ± 0.60
	17	1.94 ± 0.05	3.84 ± 0.10	7.69 ± 0.22	15.54 ± 0.41
	18	1.74 ± 0.04	3.86 ± 0.12	8.00 ± 0.00	16.00 ± 0.00
	19	1.99 ± 0.06	4.02 ± 0.11	8.10 ± 0.21	16.19 ± 0.35
	20	2.02 ± 0.05	4.09 ± 0.09	8.21 ± 0.18	16.30 ± 0.25
ResNet-34	1	1.99 ± 0.12	3.87 ± 0.26	7.73 ± 0.44	15.51 ± 1.01
	2	2.01 ± 0.06	3.87 ± 0.12	7.99 ± 0.33	15.25 ± 0.85
	3	1.96 ± 0.05	3.75 ± 0.10	7.65 ± 0.28	15.35 ± 0.51
	4	1.96 ± 0.05	3.78 ± 0.11	7.83 ± 0.25	15.54 ± 0.58
	5	1.93 ± 0.05	3.71 ± 0.12	7.56 ± 0.26	15.56 ± 0.49
	6	1.96 ± 0.05	3.76 ± 0.11	7.65 ± 0.23	15.72 ± 0.57
	7	1.94 ± 0.05	3.74 ± 0.11	7.58 ± 0.24	15.80 ± 0.45
	8	2.01 ± 0.05	3.90 ± 0.11	7.72 ± 0.21	16.27 ± 0.52
	9	1.83 ± 0.05	3.52 ± 0.11	7.45 ± 0.28	14.83 ± 0.58
	10	1.69 ± 0.06	3.49 ± 0.17	8.00 ± 0.01	16.00 ± 0.00
	11	1.89 ± 0.05	3.69 ± 0.11	7.61 ± 0.22	15.60 ± 0.52
	12	1.93 ± 0.05	3.76 ± 0.12	7.69 ± 0.25	15.81 ± 0.49
	13	1.95 ± 0.05	3.79 ± 0.10	7.72 ± 0.21	15.95 ± 0.52
	14	1.99 ± 0.05	3.89 ± 0.12	7.85 ± 0.24	16.16 ± 0.52
	15	1.97 ± 0.05	3.85 ± 0.11	7.77 ± 0.21	16.06 ± 0.52
	16	2.03 ± 0.05	3.98 ± 0.11	7.98 ± 0.23	16.39 ± 0.52
	17	2.06 ± 0.06	4.07 ± 0.12	7.91 ± 0.23	16.67 ± 0.51
	18	1.80 ± 0.07	3.59 ± 0.12	7.41 ± 0.21	15.41 ± 0.56
	19	1.65 ± 0.05	3.48 ± 0.14	8.00 ± 0.01	16.00 ± 0.00
	20	1.93 ± 0.06	3.87 ± 0.11	7.78 ± 0.21	16.29 ± 0.51
	21	2.01 ± 0.06	4.03 ± 0.10	8.04 ± 0.21	16.45 ± 0.53
	22	2.00 ± 0.06	4.00 ± 0.10	8.01 ± 0.20	16.49 ± 0.56
	23	2.05 ± 0.06	4.10 ± 0.10	8.19 ± 0.21	16.59 ± 0.52
	24	2.04 ± 0.05	4.06 ± 0.10	8.12 ± 0.20	16.57 ± 0.55
	25	2.03 ± 0.06	4.11 ± 0.12	8.23 ± 0.24	16.83 ± 0.51
	26	2.05 ± 0.05	4.08 ± 0.10	8.15 ± 0.20	16.59 ± 0.53
	27	2.02 ± 0.07	4.09 ± 0.13	8.24 ± 0.27	16.89 ± 0.52
	28	2.05 ± 0.06	4.08 ± 0.11	8.14 ± 0.20	16.51 ± 0.52
	29	2.02 ± 0.06	4.11 ± 0.13	8.32 ± 0.28	16.86 ± 0.50
	30	2.16 ± 0.06	4.31 ± 0.10	8.39 ± 0.20	17.12 ± 0.61
	31	1.95 ± 0.05	3.86 ± 0.09	7.75 ± 0.19	15.63 ± 0.37
	32	1.79 ± 0.04	3.95 ± 0.11	8.00 ± 0.00	16.00 ± 0.00
	33	1.98 ± 0.05	3.99 ± 0.10	8.05 ± 0.19	16.12 ± 0.29
	34	2.02 ± 0.04	4.06 ± 0.08	8.16 ± 0.18	16.26 ± 0.26
	35	1.97 ± 0.06	3.98 ± 0.11	8.01 ± 0.21	16.01 ± 0.27
	36	2.07 ± 0.05	4.14 ± 0.10	8.25 ± 0.30	16.22 ± 0.45
VGG-16	1	2.07 ± 0.09	4.08 ± 0.17	8.22 ± 0.37	16.62 ± 0.85
	2	2.00 ± 0.06	3.90 ± 0.12	7.77 ± 0.25	15.88 ± 0.63
	3	1.98 ± 0.05	3.88 ± 0.13	7.95 ± 0.31	15.51 ± 0.80
	4	1.98 ± 0.06	3.83 ± 0.13	7.69 ± 0.26	15.60 ± 0.60
	5	1.96 ± 0.06	3.86 ± 0.13	7.94 ± 0.26	15.43 ± 0.68
	6	1.94 ± 0.07	3.82 ± 0.13	7.80 ± 0.25	15.87 ± 0.55
	7	1.94 ± 0.06	3.81 ± 0.12	7.69 ± 0.22	15.94 ± 0.58
	8	1.98 ± 0.06	3.93 ± 0.11	7.94 ± 0.26	15.94 ± 0.69
	9	2.02 ± 0.06	4.04 ± 0.10	8.07 ± 0.24	16.17 ± 0.67
	10	1.98 ± 0.07	3.98 ± 0.12	7.91 ± 0.18	16.59 ± 0.90
	11	1.91 ± 0.08	3.88 ± 0.12	7.80 ± 0.23	15.78 ± 0.44
	12	2.01 ± 0.06	4.06 ± 0.11	8.09 ± 0.20	16.19 ± 0.35
	13	2.00 ± 0.05	4.01 ± 0.09	8.00 ± 0.20	15.95 ± 0.43
ConvNeXt-T	1	2.06 ± 0.11	3.99 ± 0.15	7.97 ± 0.39	15.71 ± 0.95
	2	1.88 ± 0.06	3.66 ± 0.15	7.09 ± 0.34	14.47 ± 0.55
	3	1.86 ± 0.06	3.59 ± 0.16	7.04 ± 0.31	14.33 ± 0.54
	4	1.86 ± 0.07	3.61 ± 0.16	7.00 ± 0.35	14.43 ± 0.56
	5	1.96 ± 0.07	3.99 ± 0.15	7.88 ± 0.34	15.71 ± 0.54
	6	1.84 ± 0.08	3.77 ± 0.14	7.61 ± 0.29	15.41 ± 0.55
	7	1.83 ± 0.10	3.72 ± 0.16	7.53 ± 0.32	15.27 ± 0.60
	8	1.80 ± 0.09	3.72 ± 0.19	7.65 ± 0.29	15.38 ± 0.56
	9	1.83 ± 0.07	3.61 ± 0.24	6.93 ± 0.48	14.20 ± 0.71
	10	1.93 ± 0.07	3.89 ± 0.15	7.85 ± 0.23	16.00 ± 0.00
	11	1.94 ± 0.07	3.87 ± 0.16	7.83 ± 0.23	16.00 ± 0.00
	12	1.95 ± 0.08	3.78 ± 0.19	7.70 ± 0.35	16.00 ± 0.00
	13	1.95 ± 0.07	3.90 ± 0.17	7.89 ± 0.26	16.00 ± 0.00
	14	1.93 ± 0.07	3.85 ± 0.17	7.82 ± 0.26	16.00 ± 0.00
	15	1.96 ± 0.07	3.93 ± 0.14	7.88 ± 0.20	16.00 ± 0.00
	16	1.97 ± 0.07	3.91 ± 0.15	7.88 ± 0.25	16.00 ± 0.00
	17	1.97 ± 0.07	3.93 ± 0.14	7.90 ± 0.20	16.00 ± 0.00
	18	2.01 ± 0.06	3.97 ± 0.14	7.98 ± 0.18	16.00 ± 0.00
	19	1.83 ± 0.06	3.64 ± 0.13	7.32 ± 0.26	15.08 ± 0.46
	20	2.00 ± 0.00	4.00 ± 0.00	8.00 ± 0.00	16.00 ± 0.00
	21	2.00 ± 0.00	4.00 ± 0.00	8.00 ± 0.00	16.00 ± 0.00
	22	2.00 ± 0.00	4.00 ± 0.00	8.00 ± 0.00	16.00 ± 0.00

Table 3: **Layer-wise p-distribution of TinyImageNet-trained L_p-masks**All values (Median ± Stdev) are calculated with p of all L_p-masks in each layer, from 5 different trials of TinyImageNet-trained models.

TinyImageNet

Model	**Layer**	**L_p-Conv (p=2)**	**L_p-Conv (p=4)**	**L_p-Conv (p=8)**	**L_p-Conv (p=16)**
AlexNet	1	1.91 ± 0.22	3.62 ± 0.31	7.21 ± 0.41	14.57 ± 0.89
	2	1.99 ± 0.06	3.91 ± 0.28	7.52 ± 0.70	15.21 ± 1.33
	3	1.91 ± 0.11	3.46 ± 0.25	7.15 ± 0.66	14.78 ± 1.34
	4	1.71 ± 0.16	2.97 ± 0.37	6.51 ± 0.58	13.86 ± 0.91
	5	1.70 ± 0.18	2.82 ± 0.47	6.34 ± 0.75	13.41 ± 1.14
ResNet-18	1	2.12 ± 0.33	4.04 ± 0.41	7.92 ± 0.70	15.93 ± 1.82
	2	2.07 ± 0.08	4.02 ± 0.17	7.83 ± 0.49	16.56 ± 1.32
	3	1.98 ± 0.08	3.75 ± 0.17	7.36 ± 0.39	16.97 ± 1.42
	4	1.99 ± 0.09	3.75 ± 0.17	7.35 ± 0.36	16.92 ± 1.29
	5	1.98 ± 0.08	3.68 ± 0.18	7.19 ± 0.30	17.19 ± 1.26
	6	2.02 ± 0.10	3.85 ± 0.18	7.45 ± 0.28	17.52 ± 1.29
	7	1.84 ± 0.11	3.35 ± 0.22	6.77 ± 0.42	15.33 ± 1.00
	8	1.90 ± 0.08	4.05 ± 0.23	8.83 ± 0.31	17.29 ± 0.32
	9	1.89 ± 0.12	3.48 ± 0.25	7.06 ± 0.43	15.96 ± 1.07
	10	1.98 ± 0.10	3.63 ± 0.24	7.17 ± 0.41	16.97 ± 1.20
	11	2.02 ± 0.11	3.82 ± 0.23	7.40 ± 0.37	17.15 ± 1.18
	12	1.82 ± 0.11	3.30 ± 0.23	6.71 ± 0.35	15.50 ± 1.02
	13	1.75 ± 0.06	3.77 ± 0.18	8.64 ± 0.25	17.16 ± 0.27
	14	1.84 ± 0.12	3.39 ± 0.23	7.07 ± 0.37	16.47 ± 1.08
	15	1.93 ± 0.12	3.57 ± 0.28	7.24 ± 0.42	17.77 ± 1.15
	16	2.01 ± 0.11	3.82 ± 0.24	7.56 ± 0.41	17.49 ± 1.10
	17	1.75 ± 0.08	3.19 ± 0.16	6.68 ± 0.26	15.60 ± 0.70
	18	1.82 ± 0.06	4.28 ± 0.17	9.25 ± 0.18	17.59 ± 0.16
	19	1.78 ± 0.10	3.25 ± 0.16	7.18 ± 0.38	17.55 ± 0.96
	20	1.69 ± 0.06	3.57 ± 0.13	8.29 ± 0.27	18.37 ± 0.67
ResNet-34	1	2.11 ± 0.24	4.02 ± 0.36	7.92 ± 0.59	15.75 ± 1.97
	2	2.10 ± 0.08	4.04 ± 0.17	7.93 ± 0.50	16.90 ± 1.29
	3	2.04 ± 0.09	3.87 ± 0.20	7.48 ± 0.53	17.23 ± 1.30
	4	2.04 ± 0.09	3.88 ± 0.19	7.50 ± 0.49	17.14 ± 1.28
	5	2.02 ± 0.09	3.80 ± 0.22	7.36 ± 0.40	17.41 ± 1.27
	6	2.02 ± 0.08	3.80 ± 0.17	7.39 ± 0.35	17.48 ± 1.32
	7	2.05 ± 0.08	3.83 ± 0.19	7.35 ± 0.43	17.65 ± 1.18
	8	2.10 ± 0.10	3.96 ± 0.17	7.53 ± 0.32	18.15 ± 1.33
	9	1.87 ± 0.12	3.46 ± 0.25	6.93 ± 0.53	15.58 ± 0.98
	10	1.86 ± 0.07	3.93 ± 0.20	8.67 ± 0.30	17.14 ± 0.30
	11	1.87 ± 0.12	3.54 ± 0.24	7.21 ± 0.44	16.33 ± 1.07
	12	1.96 ± 0.13	3.67 ± 0.28	7.27 ± 0.48	17.16 ± 1.17
	13	1.96 ± 0.12	3.67 ± 0.22	7.34 ± 0.42	17.24 ± 1.21
	14	2.06 ± 0.11	3.88 ± 0.25	7.64 ± 0.55	17.96 ± 1.18
	15	1.98 ± 0.11	3.75 ± 0.22	7.48 ± 0.38	17.63 ± 1.25
	16	2.12 ± 0.12	4.05 ± 0.25	7.98 ± 0.61	18.33 ± 1.11
	17	2.11 ± 0.13	4.03 ± 0.24	7.62 ± 0.50	18.18 ± 1.24
	18	1.88 ± 0.12	3.47 ± 0.26	6.90 ± 0.42	15.96 ± 1.15
	19	1.73 ± 0.06	3.73 ± 0.18	8.61 ± 0.25	17.13 ± 0.26
	20	1.89 ± 0.12	3.52 ± 0.24	7.20 ± 0.39	16.64 ± 1.10
	21	1.94 ± 0.15	3.56 ± 0.32	7.27 ± 0.51	17.63 ± 1.20
	22	1.90 ± 0.11	3.61 ± 0.21	7.40 ± 0.38	17.34 ± 1.13
	23	1.99 ± 0.12	3.81 ± 0.27	7.55 ± 0.53	18.43 ± 1.07
	24	1.87 ± 0.11	3.64 ± 0.19	7.57 ± 0.34	17.72 ± 1.07
	25	2.00 ± 0.10	3.92 ± 0.22	7.91 ± 0.47	18.69 ± 0.85
	26	1.85 ± 0.09	3.71 ± 0.16	7.69 ± 0.29	17.94 ± 0.95
	27	2.03 ± 0.09	4.02 ± 0.20	8.18 ± 0.48	18.64 ± 0.82
	28	1.86 ± 0.08	3.77 ± 0.16	7.79 ± 0.27	17.98 ± 0.88
	29	2.07 ± 0.10	4.11 ± 0.21	8.35 ± 0.53	18.54 ± 0.83
	30	1.95 ± 0.09	3.90 ± 0.20	7.69 ± 0.38	18.75 ± 1.07
	31	1.98 ± 0.10	3.71 ± 0.21	7.31 ± 0.29	15.82 ± 0.70
	32	1.86 ± 0.07	4.41 ± 0.22	9.44 ± 0.21	17.74 ± 0.18
	33	1.82 ± 0.09	3.31 ± 0.16	6.90 ± 0.30	16.64 ± 1.02
	34	1.88 ± 0.09	3.55 ± 0.19	7.43 ± 0.29	18.29 ± 1.02
	35	1.87 ± 0.12	3.47 ± 0.19	7.54 ± 0.41	17.82 ± 0.97
	36	1.90 ± 0.06	3.78 ± 0.13	8.07 ± 0.26	18.92 ± 0.69
VGG-16	1	2.07 ± 0.16	4.11 ± 0.24	8.29 ± 0.72	17.52 ± 1.71
	2	2.15 ± 0.10	4.17 ± 0.21	8.18 ± 0.52	17.27 ± 1.11
	3	2.08 ± 0.11	4.09 ± 0.23	7.99 ± 0.54	17.38 ± 1.30
	4	2.15 ± 0.10	4.12 ± 0.21	7.92 ± 0.49	17.76 ± 1.16
	5	1.95 ± 0.10	3.79 ± 0.22	7.65 ± 0.52	17.52 ± 1.39
	6	1.98 ± 0.12	3.78 ± 0.29	7.55 ± 0.56	18.26 ± 1.25
	7	2.04 ± 0.14	3.98 ± 0.31	7.72 ± 0.60	18.05 ± 1.36
	8	1.95 ± 0.13	3.72 ± 0.30	7.50 ± 0.54	16.84 ± 1.32
	9	1.91 ± 0.14	3.68 ± 0.29	7.69 ± 0.48	18.04 ± 1.27
	10	2.00 ± 0.15	3.90 ± 0.29	7.91 ± 0.50	18.38 ± 1.64
	11	1.82 ± 0.11	3.43 ± 0.19	7.28 ± 0.36	16.61 ± 1.28
	12	1.83 ± 0.10	3.51 ± 0.18	7.52 ± 0.27	16.78 ± 1.29
	13	1.96 ± 0.07	3.86 ± 0.14	7.64 ± 0.26	16.09 ± 0.80
ConvNeXt-T	1	1.98 ± 0.20	4.01 ± 0.37	8.16 ± 1.06	16.22 ± 2.12
	2	1.95 ± 0.10	3.70 ± 0.22	7.42 ± 0.49	14.91 ± 0.92
	3	1.97 ± 0.11	3.71 ± 0.21	7.26 ± 0.45	14.63 ± 0.93
	4	1.96 ± 0.12	3.68 ± 0.23	7.25 ± 0.45	15.15 ± 0.99
	5	1.88 ± 0.15	3.92 ± 0.36	7.66 ± 1.09	15.48 ± 2.55
	6	1.94 ± 0.11	3.65 ± 0.22	7.11 ± 0.44	14.38 ± 1.01
	7	1.96 ± 0.09	3.58 ± 0.22	7.01 ± 0.48	13.86 ± 0.88
	8	1.95 ± 0.11	3.59 ± 0.24	7.02 ± 0.45	14.12 ± 0.96
	9	1.83 ± 0.13	3.71 ± 0.47	7.11 ± 1.02	14.22 ± 2.32
	10	1.94 ± 0.09	3.51 ± 0.20	6.64 ± 0.43	13.76 ± 0.89
	11	1.93 ± 0.09	3.50 ± 0.20	6.68 ± 0.42	13.87 ± 0.84
	12	1.93 ± 0.10	3.50 ± 0.20	6.62 ± 0.40	13.56 ± 0.84
	13	1.94 ± 0.11	3.54 ± 0.20	6.64 ± 0.39	13.75 ± 0.80
	14	1.94 ± 0.10	3.53 ± 0.21	6.66 ± 0.40	13.68 ± 0.77
	15	1.93 ± 0.11	3.56 ± 0.22	6.71 ± 0.40	13.75 ± 0.75
	16	1.94 ± 0.11	3.58 ± 0.19	6.80 ± 0.40	14.14 ± 0.85
	17	1.94 ± 0.11	3.59 ± 0.29	7.03 ± 0.42	14.44 ± 0.88
	18	1.95 ± 0.10	3.61 ± 0.25	7.01 ± 0.39	14.55 ± 0.80
	19	1.74 ± 0.08	3.64 ± 0.25	7.32 ± 0.51	15.15 ± 1.17
	20	1.87 ± 0.10	3.62 ± 0.21	7.20 ± 0.34	14.69 ± 0.77
	21	1.87 ± 0.10	3.65 ± 0.19	7.21 ± 0.35	14.55 ± 0.77
	22	1.92 ± 0.09	3.77 ± 0.17	7.45 ± 0.33	15.02 ± 0.76

A.18 Learned L_p-mask properties (p=16)

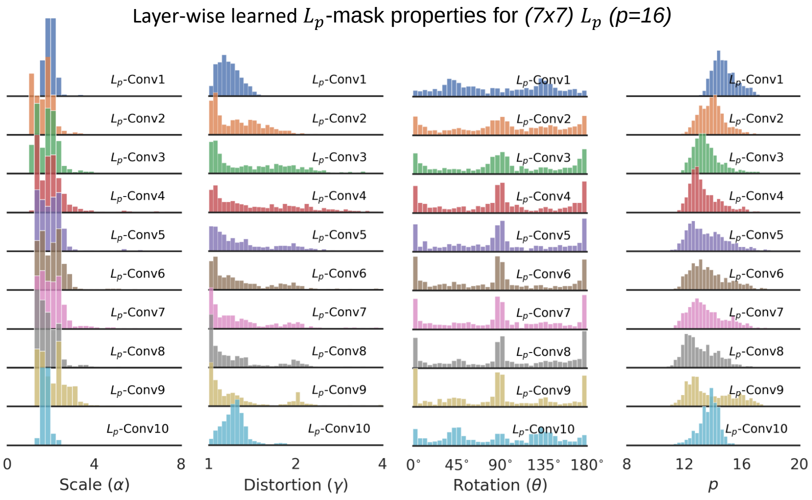

Figure 16: **Layer-wise distribution of learned L_p-mask properties (p=16)**

A.19 Statistics for comparison of optimized MPND p values in artificial and biological RFs

Table 4: Holm-Bonferroni corrected multiple comparisons of each RFs using Welch's t-test. Lower diagonal elements denote corrected statistical p-values and upper diagonal elements denote degree of significance (n.s, not significant; *, 0.01<p<0.05; **, 0.001<p<0.01; ***, p<0.001;)

Welch's t-test (corrected p-values)	**Mouse V1 Layer 2/3**	**Trained + Image**	**Trained + Noise**	**Untrained + Noise**	**Untrained + Image**
Mouse V1 Layer 2/3	-	*	*	***	***
Trained + Image	1.10e-2	-	n.s	***	***
Trained + Noise	1.06e-2	7.6e-1	-	***	***
Untrained + Noise	1.23e-15	4.13e-28	1.49e-25	-	***
Untrained + Image	8.94e-14	1.59e-25	6.73e-23	1.39e-22	-

A.20 Impact of L_p-Convolution (p=2) on other CNN architectures

Table 5: Top-1 performance (mean±std, 5 trials) on the CIFAR-100 datasets with L_p-Convolution applied in ConvNeXt-V2-T (Woo et al., 2023), ResNet-50 (He et al., 2016), ResNext-50 (Xie et al., 2017) and DenseNet-121 (Huang et al., 2017). The symbol ✓ indicates L_p-Converted ($p_{\text{init}} = 2$) or not. '***' denotes statistical comparison using Welch's t-test ($p < 0.001$).

		CIFAR-100		
L_p-Conv	**ConvNeXt-V2-T**	**ResNet-50**	**ResNeXt-50**	**DenseNet-121**
-	64.26 ± 0.41	73.17 ± 0.23	73.55 ± 0.57	74.12 ± 0.16
✓	*** 65.58 ± 0.25	*** 76.66 ± 0.19	*** 77.38 ± 0.36	*** 77.14 ± 0.18